The MSXX Force Field for the Barium Sulfate−Water Interface

Yun Hee Jang,[†,‡] Xiao Yan Chang,[†] Mario Blanco,[†] Sungu Hwang,[†,‡] Yongchun Tang,[§] Patrick Shuler,[§] and William A. Goddard III*,[†]

Materials and Process Simulation Center, Beckman Institute (139-74), California Institute of Technology, Pasadena, California 91125, and Chevron Petroleum Technology Company, 2811 Hayes Road, Houston, Texas 77082

Received: September 5, 2001; In Final Form: April 3, 2002

A new force field (MSXX FF) was developed for barium sulfate ($BaSO_4$) to reproduce the experimental properties of $BaSO_4$ crystal (density, lattice energy, compressibility, and vibrational spectrum) and to describe properly the interaction between $BaSO_4$ and water (binding energies and interatomic distances of $Ba(H_2O)_8^{2+}$ and $(SO_4)(H_2O)_6^{2-}$ clusters determined from ab initio quantum mechanics calculations). Using this FF in combination with F3C FF for water, the surface energies for several surfaces of $BaSO_4$ were examined both in a vacuum and in the presence of an explicit water bath in contact with them. The same level of FF's are also reported for $CaSO_4$ and $SrSO_4$.

1. Introduction

In secondary oil recovery, seawater is injected into the reservoir to maintain oil pressure. The seawater contains SO_4^{2-}, and the water in the oil formation often contains high concentrations of Ba^{2+}, Ca^{2+}, and Sr^{2+}. As a result, highly insoluble alkaline earth metal sulfates [barite ($BaSO_4$), celestite ($SrSO_4$), and anhydrite ($CaSO_4$)] form an unwanted precipitate (scale) that blocks production tubing in off-shore oil-fields.[1−6] Especially, $BaSO_4$ represents a major scale problem because of its exceedingly low solubility.[4,7,8] This had led to significant effort toward developing chemicals to inhibit crystal growth (scale inhibitors) or to dissolve already-grown crystals (scale dissolvers).[7,9,10] There have been many experiments to understand the morphology of barite crystals,[11] the nucleation and crystal growth process of barite,[12,13] and the morphology and growth rate of etch pits generated during the dissolution of barite.[14−21] These processes are known to be affected by organic and inorganic additives[22−26] or surfactants,[27] which should provide insight for the rational design of more efficient inhibitors and dissolvers.

Several theoretical studies have modeled these problems.[28−33] Hartman−Perdok theory [periodic bond chain (PBC) theory] with an electrostatic point-charge model[28] has been used to explain the morphology of $BaSO_4$ crystals,[28,29] but this theory does not include dispersion [van der Waals (vdW)] interactions between atoms nor the effects of surface relaxation and reconstruction.[34] Allan and co-workers[30] developed a force field (FF) for $BaSO_4$ including dispersion interactions, and this FF was used by Allan and co-workers,[30] Rohl and co-workers,[32,35] and Parker and co-workers[31,33] to calculate surface energies of various surfaces and predict the morphology of these crystals while including surface relaxation. Their surface energies were in the order

$$(001) < (210) < (211) < (010) < (101) < (100) < (011)$$

for unrelaxed surfaces and

$$(210) < (001) < (211) < (101) < (010) < (100) < (011)$$

for relaxed surfaces. This led to a predicted crystal morphology mostly bound by (001) and (210) faces in agreement with the experimentally observed morphology. Blanco and co-workers[36] obtained similar results, with an early version of the FF being reported here.

The previous theoretical studies have several limitations. First, they focused on solid−vacuum interfaces, whereas most growth and dissolution processes are carried out in aqueous media.[34] That is, the previous studies did not involve the solvent−surface interactions, which are likely to be important for ionic crystals.[37] Indeed, it has been proposed that the precipitation kinetics is governed by the dehydration frequency of metal ions and that the dissolution kinetics is governed by solvation affinity for the near-surface divalent metals.[38] For both growth and dissolution, the solvation of surface atoms especially on steps or on kinks is the controlling factor. Thus, inclusion of the solvent in theory is essential for comparing to experiment.

Second, the FF parameters in the previous studies were fitted by matching the structure and elastic properties calculated for a minimized structure (using molecular mechanics (MM), that is, at 0 K) to the experimental structure and properties obtained at room temperature. This is not quite consistent because molecular dynamics (MD) at 298 K would lead to the expansion of the crystal and, hence, modified properties. Previously, surface relaxation was calculated only by minimization at 0 K, leading to just one local minimum configuration, which might bias the results. For an accurate comparison to the experiment, it is important to use MD or Monte Carlo simulation at the appropriate temperature.[31] Indeed, Parker and co-workers[33] commented that "in the future, we would like to study the effect of water on the growth of barium sulfate surfaces, using both static calculations and molecular dynamics".

* To whom correspondence should be addressed. E-mail: wag@wag.caltech.edu.
† California Institute of Technology.
‡ Present address: School of Chemistry, Seoul National University, Seoul 151-747, Korea.
§ Chevron Petroleum Technology Company.

10.1021/jp0133900 CCC: $22.00
Published on Web 08/31/2002

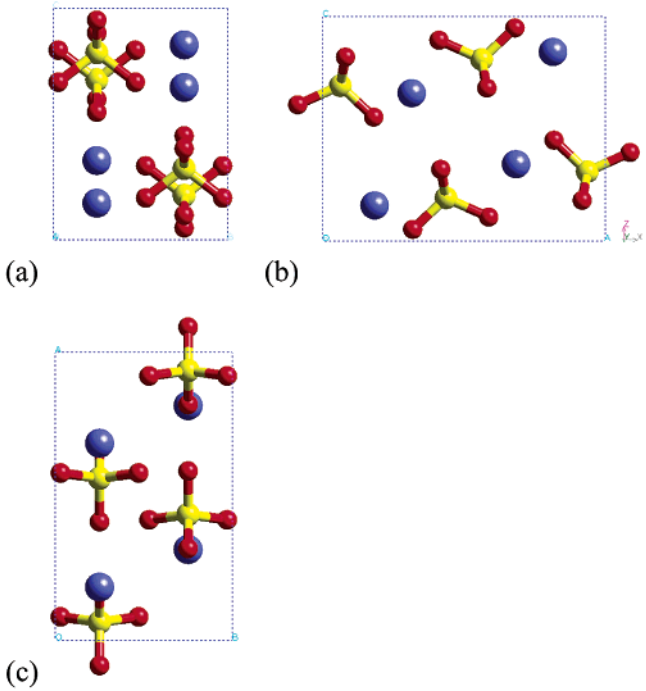

Figure 1. Unit cell of $BaSO_4$. (a) Projected along the [100] direction, (b) along [010], and (c) along [001]. Here the biggest ball represents Ba^{2+}, whereas the smaller balls represent S and O in SO_4^{2-}.

The present work develops the new MSXX FF for $BaSO_4$ (also for $CaSO_4$ and $SrSO_4$) such that MD at 298 K reproduces experimental properties at room temperature. We expect this FF to accurately model scale inhibition or dissolution, because the FF describes well both the sulfate crystal and the interaction of $BaSO_4$ with water and other moieties constituting the scale problem (inhibitor and/or dissolver) at room temperature.

Section 2 documents the experimental data to which we fitted the FF. This includes crystal structure (density and lattice constants), energetics (lattice energy or cohesive energy), elastic properties (compressibility or elastic constants or bulk modulus), and vibrational frequencies. Section 3 describes the form of the MSXX FF for $BaSO_4$ and determines the charges from quantum mechanical (QM) calculations. Section 4 develops the FF parameters for $BaSO_4$ by comparing MD (at 298 K) to the experiment. Section 5 summarizes the FF used for water. Section 6 reports QM calculations on $Ba(H_2O)_8^{2+}$ and $(SO_4)(H_2O)_6^{2-}$ clusters, which are used to extract FF to describe the interactions of Ba^{2+} and SO_4^{2-} with water. This FF is used in section 7 for MD simulations of the energies of various water−barite interfaces at room temperature. Finally, a summary is given in section 8.

2. Experimental Properties of $BaSO_4$

2.1. Crystal Cell Parameters. Barite has an orthorhombic crystal structure with the *Pnma* (D^{16}_{2h}, no. 62) space group and lattice constants of $a = 8.8842$ Å, $b = 5.4559$ Å, $c = 7.1569$ Å at 21 °C (density $\rho = 4.474$ g/cm^3; Figure 1).[38,39] Each Ba^{2+} has six nearest-neighbor SO_4^{2-}'s leading to 12 oxygen atoms in the first nearest-neighbor oxygen shell with distances ranging from 2.765 to 3.315 Å. The Ba−S nearest-neighbor distances are 3.51−3.96 Å. The S−O distance is 1.483−1.497 Å (mean = 1.487 Å).

2.2. Lattice Energy. The lattice energy (or cohesive energy) of $BaSO_4$ is defined as the enthalpy change for the process

$$BaSO_4(cr) \rightarrow Ba^{2+}(g) + SO_4^{2-}(g) \qquad (1)$$

TABLE 1: Experimental Dissolution Enthalpies of MSO_4 (M = Ba, Sr, and Ca; kcal/mol) at 25 °C

	$BaSO_4$	$SrSO_4$	$CaSO_4$
$\Delta H_f^0[MSO_4(cr)]^a$	−352.1	−347.3	−342.8
$\Delta H_f^0[M^{2+}(aq)]^a$	−128.5	−130.4	−129.7
$\Delta H_f^0[SO_4^{2-}(aq)]^a$	−217.3	−217.3	−217.3
ΔH_{diss} in eq 3	6.3	−0.4	−4.2
$\log K_{sp}{}^{b-c}$	−9.967[b]	−6.464[b]	−4.307[b]
	−9.959[c]	−6.613[c]	−4.265[c]

[a] References 4−6, 40, and 41. [b] $K_{sp} = [M^{2+}]_{aq}[SO_4^{2-}]_{aq}$ = solubility product. Reference 40. [c] References 4−6.

TABLE 2: Experimental Hydration Enthalpies of M^{2+} (M = Ba, Sr, and Ca) and SO_4^{2-} at 25 °C

	Ba^{2+}	Sr^{2+}	Ca^{2+}	SO_4^{2-}
$\Delta H_{hyd}(M^{2+}$ or $SO_4^{2-})^a$	−314.1	−347.0	−378.6	−272 (±12)
$\Delta H_{hyd}(M^{2+}$ or $SO_4^{2-})^b$	−320	−353	−386	−265 ± 12
$\Delta H_{hyd}(M^{2+}$ or $SO_4^{2-})^c$	−325.47	−359.22	−394.50	
$\Delta H_{dehyd}(MSO_4)$ in eq 4a	586 ± 12	619 ± 12	651 ± 12	

[a] Reference 42. [b] Reference 43. [c] Reference 44.

There is no direct experimental way to measure this enthalpy change. Thus, we partition this process into two separate paths for which enthalpy changes can be obtained from experiments

$$BaSO_4(cr) \rightarrow Ba^{2+}(aq) + SO_4^{2-}(aq) \qquad (2a)$$

$$Ba^{2+}(aq) + SO_4^{2-}(aq) \rightarrow Ba^{2+}(g) + SO_4^{2-}(g) \qquad (2b)$$

The enthalpy change of the above step (2a) corresponds to the dissolution enthalpy of $BaSO_4$:

$$\Delta H_{diss} = \Delta H_f^0[Ba^{2+}(aq)] + \Delta H_f^0[SO_4^{2-}(aq)] - \Delta H_f^0[BaSO_4(cr)] \qquad (3)$$

Using the standard heat of formation of each species (Table 1),[4−6,40,41] we estimate ΔH_{diss} as 6.3 kcal/mol for $BaSO_4$, −0.4 kcal/mol for $SrSO_4$, and −4.2 kcal/mol for $CaSO_4$ (Table 1) as estimated by Raju and co-workers.[4−6] This shows a good correlation with the observed solubility of each sulfate in water, that is, the more negative ΔH_{diss} (in turn the more negative ΔG_{diss}) for the more soluble sulfate salts (that is, the higher solubility product (K_{sp}) where $K_{sp} = [M^{2+}]_{aq}[SO_4^{2-}]_{aq}$; Table 1) according to the relationship

$$-\Delta G_{diss} = RT \ln K_{sp}$$

The enthalpy change during the step (2b) is the negative sum of hydration energies of Ba^{2+} and SO_4^{2-}:

$$\Delta H_{dehyd} = -\Delta H_{hyd}(Ba^{2+}) - \Delta H_{hyd}(SO_4^{2-}) \qquad (4a)$$

The hydration enthalpies of Ba^{2+}, Sr^{2+}, Ca^{2+}, and SO_4^{2-} listed in Table 2 were taken from the tabulations of Marcus[42] and others.[43,44] The conventional enthalpy of hydration assumes the heat of formation of $H^+(aq)$ in the aqueous phase is zero (standard state)

$$\Delta H_{hyd}(H^+) = 0 \qquad (4b)$$

The absolute enthalpy of hydration listed in Table 2 is estimated from the conventional one by

$$\Delta H_{hyd}(I^z) = \Delta H_{hyd,conv}(I^z) + z\,\Delta H_{hyd}(H^+) \qquad (4c)$$

TABLE 3: Estimated Experimental Lattice Energies of MSO_4 (M = Ba, Sr, and Ca; kcal/mol) at 25 °C

	$BaSO_4$	$SrSO_4$	$CaSO_4$
ΔH_{diss} [Table 1]	6.3	−0.4	−4.2
ΔH_{dehyd} [Table 2]	586 (±12)	619 (±12)	651 (±12)
ΔH_{latt} [eq 5]	592 (±12)	619 (±12)	647 (±12)

where z is the charge of the ion I. The absolute hydration enthalpy of the proton $\Delta H_{hyd}(H^+)$ is still uncertain,[42,45−48] with values ranging from −261 to −275 kcal/mol. The variation between values for $\Delta H_{hyd}(I^z)$ taken from different references (Table 2) is mostly due to the different values for $\Delta H_{hyd}(H^+)$. Fortunately, however, in determining ΔH_{dehyd} of eq 4a, this uncertainty from $\Delta H_{hyd}(H^+)$ cancels. The big uncertainty in eq 4a is in $\Delta H_{dehyd}(SO_4^{2-})$.

Combining these results (ΔH_{diss} and ΔH_{dehyd} from eq 3 and eq 4a, respectively), we estimate the lattice energy

$$\Delta H_{latt}(MSO_4) = \Delta H_{diss}(MSO_4) + \Delta H_{dehyd}(MSO_4) \quad (5)$$

as 592 (±12) kcal/mol for $BaSO_4$, 618 (±12) kcal/mol for $SrSO_4$, and 646 (±12) kcal/mol for $CaSO_4$ (Table 3). The lattice energy has previously been calculated for these sulfates from the Madelung constant,[49−51] but the values cover a large range (for example, 567, 578, and 626.4 kcal/mol for $BaSO_4$) and do not agree with our best estimate of the lattice energy (for example, (592 ± 12) − $2RT$ = 578 to 603 kcal/mol for $BaSO_4$ at 25 °C).

2.3. Compressibility. The compressibility, χ, is defined[52,53] as the change of volume produced by unit change of pressure, that is

$$\chi = \frac{1}{V_0}\left(\frac{dV}{dP}\right)_{V=V_0} \quad (6)$$

where V_0 is the volume at the standard pressure (1 bar) and temperature (298 K). It is related to the elastic constants by the relations[54,55]

$$\chi = B_{Reuss}^{-1} = s_{11} + s_{22} + s_{33} + (2s_{12} + 2s_{13} + 2s_{23}) \quad (7a)$$

or

$$\chi = B_{Voight}^{-1} = \left[\frac{1}{9}(c_{11} + c_{22} + c_{33} + 2c_{12} + 2c_{13} + 2c_{23})\right]^{-1} \quad (7b)$$

where B is the bulk modulus, the c_{ij}'s denote elements of the elastic stiffness matrix **c**, and the s_{ij}'s are elements of the compliance matrix $\mathbf{s} = \mathbf{c}^{-1}$. The experimental compressibilities of $BaSO_4$ obtained from eqs 6−7 range from 0.0170 to 0.0192 GPa^{-1} (Table 4).[53,56−64]

2.4. Vibrational Frequencies. Experimental frequencies of the internal vibration modes for single-crystal $BaSO_4$ are tabulated in Table 5. These were obtained from various sources of infrared and Raman spectra.[65−70] The SO stretching modes are $\nu_1(A)$, the totally symmetric breathing mode of SO_4^{2-} at 983−986 cm^{-1} (Raman and weak IR),[65−68] and $\nu_3(T_2)$, the asymmetric stretching mode at around 1100 cm^{-1}. The OSO bending modes are $\nu_2(E)$, the scissoring mode at 451−462 cm^{-1} (Raman),[65,66] and $\nu_4(T_2)$, the rocking mode at around 620 cm^{-1} (Table 5 and Figure 2).[65−70]

3. MSXX Force Field for $BaSO_4$

The functional form of the new FF is based on Dreiding FF[71] and given in Table 6. The bond−bond cross term E^{RR} was added to describe the correct splitting between the $\nu_1(A)$ and $\nu_3(T_2)$ modes of SO_4^{2-}, whereas the angle−angle cross term $E^{\theta\theta}$ was added to describe the splitting between $\nu_2(E)$ and $\nu_4(T_2)$ modes of SO_4^{2-} (section 4.4). This FF is denoted as MSXX.[72−75]

For the valence FF, the six valence parameters, R_0(S−O), θ_0(O−S−O), K_R(S−O), K_θ(O−S−O), K_{RR}, and $K_{\theta\theta}$, were adjusted to reproduce the experimental geometry and vibrational spectra for SO_4^{2-} in $BaSO_4$ crystal (Table 8 and section 4.4).

The atomic charges q_i's of Ba^{2+} were fixed at its formal charge +2.0|e|, and those of S and O in SO_4^{2-} were determined as +1.544|e| and −0.886|e|, respectively, by fitting to the electrostatic potential generated from ab initio calculations

TABLE 4: Experimental Elastic Properties of $BaSO_4$ [a]

reference	1990[b]	1979[c]	1951[d]	1946[e]	1928[f]	1928[g]
c_{11} (GPa)	95.14(8)	89.0	86.2	88.3	88.3	90.7
c_{22} (GPa)	83.65(8)	81.0	91.7	78.5	78.5	80.0
c_{33} (GPa)	110.60(8)	107	108.4	103.8	105.0	107.0
c_{12} (GPa)	51.32(15)	47.9	52.3	47.7	45.1	46.8
c_{13} (GPa)	33.62(12)	31.7	35.6	28.9	26.5	27.5
c_{23} (GPa)	32.76(12)	29.8	34.1	26.9	26.5	27.3
B (GPa)	58.31(53)	55.1	58.8	52.9	52.1	53.5
χ (GPa^{-1})[h]	0.0172	0.0182	0.0170	0.0189	0.0192	0.0187

[a] We assume that the two most recent references (b and c) are the most reliable. [b] Reference 57 (1990). [c] Reference 56 (1979). [d] References 58 and 59 (1951 and 1956). [e] References 63,64 (1946, 1928). [f] Reference 60 (1928). [g] Reference 61 (1928). [h] Others: 0.0183 at 308.15 K for single crystal,[62] 0.0191,[63,64] and 0.0180.[53]

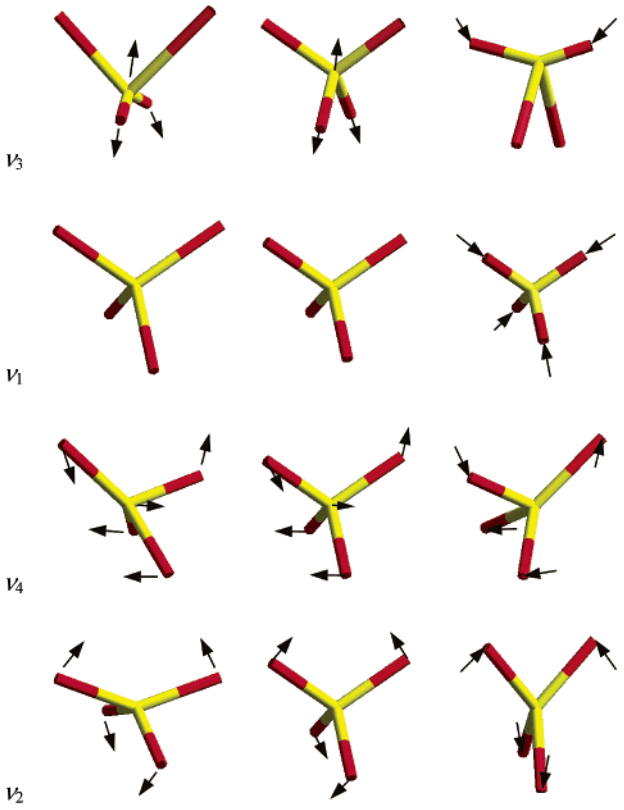

Figure 2. Internal vibration modes of SO_4 in $BaSO_4$ lattice.

TABLE 5: Internal Vibration of SO_4 in $BaSO_4$ Lattice

mode	symmetry	frequency (cm^{-1})
ν_3 (IR-, Raman-active)	T_2 (asymmetric stretching)	1107−1132
ν_1 (Raman-, IR(weak)-active)	A (symmetric stretching)	983−986
ν_4 (IR-, Raman-active)	T_2 (rocking)	615−627
ν_2 (Raman-active)	E (scissoring)	451−462

TABLE 6: Force Field for $BaSO_4$[a]

$$E = E^{\text{nonbond}} + E^{\text{valence}}$$

$$E^{\text{nonbond}} = E^{\text{coulomb}} + E^{\text{vdW}}$$

$$E^{\text{valence}} = E^{\text{bond}}_{\text{SO}} + E^{\text{angle}}_{\text{OSO}} + E^{\text{RR}}_{\text{OSO}} + E^{\theta\theta}_{\text{SOOO}}$$

$$E^{\text{coulomb}}_{\text{ij}}(R) = C_0\frac{q_i q_j}{\epsilon R_{\text{ij}}}$$

$$E^{\text{vdW}}_{\text{ij}}(R) = D_0\left\{\left[\left(\frac{6}{\zeta-6}\right)e^{\zeta(1-R/R_0)}\right] - \left[\left(\frac{\zeta}{\zeta-6}\right)\left(\frac{R_0}{R}\right)^6\right]\right\}$$

$$E^{\text{bond}}_{\text{SO}}(R) = \frac{1}{2}K_R(R-R_0)^2$$

$$E^{\text{angle}}_{\text{OSO}}(\theta) = \frac{1}{2}\frac{K_\theta}{\sin^2\theta_0}(\cos\theta - \cos\theta_0)^2$$

$$E^{\text{RR}}_{\text{OSO}}(R_1, R_2) = K_{\text{RR}}(R_1-R_0)(R_2-R_0)$$

$$E^{\theta\theta}_{\text{SOOO}}(\theta_1,\theta_2) = \frac{K_{\theta\theta}}{\sin\theta_{0_1}\sin\theta_{0_2}}(\cos\theta_1 - \cos\theta_{0_1})(\cos\theta_2 - \cos\theta_{0_2})^2$$

[a] The constants in $E^{coulomb}$ are the dielectric constant (ϵ) and $C_0 = 332.0637$ (the unit conversion factor when atomic charges q_i's are in electron units ($|e|$), the distance R is in Å, and $E^{coulomb}$ is in kcal/mol).

TABLE 7: ESP Atomic Charges in SO_4^{2-}, Which Were Calculated from the ab Initio QM Calculations in the Gas Phase and in Aqueous Solvent[a]

environment	level	basis set	r(S)/r(O)[a]	q_S ($\|e\|$)	q_O ($\|e\|$)	E_{solv} (kcal/mol)
gas-phase	B3LYP	6-31G**++		1.816	−0.954	
		6-31G**		1.121	−0.780	
		cc-pVTZ(-f)++		1.765	−0.941	
		cc-pVTZ(-f)		1.357	−0.839	
	LMP2	6-31G**		1.403	−0.851	
		LAV3P**		1.460	−0.865	
		LAV3P*		**1.544**[b]	**−0.886**[b]	
	HF	6-31G**++		2.005	−1.001	
		6-31G**		1.524	−0.881	
aqueous[a]	B3LYP	6-31G**	1.8/1.50	1.029	−0.757	−260.2
		6-31G**	1.8/1.52	1.024	−0.756	−258.7
	HF	6-31G**	1.8/1.52	1.475	−0.869	−260.4

[a] QM calculations in aqueous solvent were done with the Poisson−Boltzmann continuum solvation model[77−81] implemented in *Jaguar*.[76] The r(S) and r(O) are the parameters corresponding to the atomic vdW radii, which are used to build up the solute−solvent boundary. [b] Values selected for the FF calculations.

(*Jaguar*)[76] on SO_4^{2-} [LMP2/LAV3P* (effective core potential for S)]. This set of ESP charges are in the middle range of values from various levels of calculations (1.12|e| to 2.00|e| for S; −0.75|e| to −1.00|e| for O; Table 7).

The formal charges of Ba^{2+} and SO_4^{2-} are larger than those obtained from QM. Usually, the values from QM are about half the formal charges. Usage of formal charges on cations and anions overestimates the Coulombic energy. However, this is not an important issue here because the overestimated Coulombic interaction is balanced by the vdW interaction whose parameters (R_o, D_o, and ζ) were adjusted to reproduce the experimental structure, cohesive energy, and compressibility from the MD at 298 K (sections 4.1−4.3).

For vdW nonbonding interaction between atoms, we used a standard expontial-6 (Buckingham) form as in Table 6, whereas the FF developed by Allan and co-workers[30] employed a purely repulsive potential[82] except for the O−O interaction. No nonbonding interaction is considered for 1,2-pairs (bonded atoms) and 1,3-pairs (atoms bonded to a common atom), because it is considered that their electrostatic and vdW interactions are included in their bond and angle interactions.[71,83] The vdW parameters D_o, R_o, and ζ for oxygen and sulfur (O−O and S−S) were taken from Dreiding.[71] The vdW parameters for Ba, which are missing in the original Dreiding,[71] were adjusted to reproduce the density, lattice energy, and compressibility of the crystal (sections 4.1−4.3) with the constraint that the off-diagonal vdW parameters (Ba−O and Ba−S) are determined by the standard combination rules for vdW parameters

TABLE 8: Force Field Parameters for $BaSO_4$[a]

$E^{coulomb}$	q(Ba)	2.0|e|	q(S)	1.544|e|	q(O)	−0.886|e|
E^{vdW}	R_o(Ba)[b]	6.942	D_o(Ba)[c]	0.0012	ζ(Ba)	18.0
	R_o(S)[b]	4.0[h]	D_o(S)[c]	0.344[h]	ζ(S)	12.0[h]
	R_o(O)[b]	3.4046[h]	D_o(O)[c]	0.0957[h]	ζ(O)	13.483[h]
E^{bond}(SO)	R_o[b]	1.505	K_b[d]	955.0		
E^{angle}(OSO)	θ_o[e]	109.47	K_θ[f]	350.0		
E^{RR}(OSO)	K_{RR}[d]	102.0				
$E^{\theta\theta}$(SOOO)	$K_{\theta\theta}$[f,g]	72.5				

[a] For functional forms, see Table 6. [b] In Å. [c] In kcal/mol. [d] In kcal/mol/Å^2. [e] In degrees. [f] In kcal/mol/rad^2. [g] In the current version of *Polygraf* (version 3.30), the divisor for angle-angle cross term $E^{\theta\theta}$ is written as $E^{\theta\theta}(\cos\theta_1 - \cos\theta_{10})(\cos\theta_2 - \cos\theta_{20})$ where $E^{\theta\theta} = K_{\theta\theta}/\sin\theta_{01}\sin\theta_{02} = 81.5625$ where $K_{\theta\theta} = 72.5$. In *Cerius2*, the input is in terms of $K_{\theta\theta}$. [h] From Dreiding; ref 71.

$$E_{\text{AB}} = \alpha_{\text{AB}}e^{-\beta_{\text{AB}}R_{\text{AB}}} - \frac{\gamma_{\text{AB}}}{R_{\text{AB}}^6} \tag{8a}$$

where

$$\alpha_{\text{AB}} = \sqrt{\alpha_{\text{AA}}\alpha_{\text{BB}}}$$

$$\beta_{\text{AB}} = \frac{1}{2}(\beta_{\text{AA}} + \beta_{\text{BB}})$$

$$\gamma_{\text{AB}} = \sqrt{\gamma_{\text{AA}}\gamma_{\text{BB}}} \tag{8b}$$

The optimized FF parameters are given in Table 8, and the properties of bulk crystal with these parameters are given in the next section. The FF of Allan and co-workers[30] is also listed in Appendix C for comparison with ours. Their FF is based on minimization at 0 K rather than MD at 298 K as our FF. For a direct comparison, we carried out MD at 298 K using their FF and compared the results with ours and with experiments (Appendix C).

4. Bulk Crystal Properties

The crystallographic unit cell of $BaSO_4$ ($Z = 4$, 24 atoms; Figure 1)[38,39] was taken as a unit cell in the calculation. The crystal structure was optimized with the Newton−Raphson method using *Cerius2* software.[84] To obtain the density and other properties at room temperature, we carried out Nosé−Hoover (NPT)[85−87] Rahman−Parrinello MD simulations at 298 K and 1 bar. A time step of 1 fs was used, and properties were calculated from the average over 250 ps after 50-ps equilibration. Standard deviations were calculated from a series of averages calculated for each 25-ps block. Nonbonding interactions were estimated using the Ewald procedure where the slow convergence of the lattice sum is accelerated without sacrificing accuracy by multiplying the sum by a rapidly decreasing convergence function such as the error function and by its complementary function, with the latter term estimated in the reciprocal lattice.[88] The Ewald parameters used in the calculations are given in the footnote of Table 9.

TABLE 9: Calculated Density and Cell Parameters of $BaSO_4$

	MM (0 K)[a]	MD (298 K)[b]	expt (298 K)[c]
a (Å)	8.6634	8.720 ± 0.005	8.8842
b (Å)	5.6118	5.636 ± 0.003	5.4559
c (Å)	7.0373	7.061 ± 0.004	7.1569
α (°)	90	90.02 ± 0.03	90
β (°)	90	89.99 ± 0.04	90
γ (°)	90	90.00 ± 0.04	90
density (g/cm^3)	4.5310	4.473	4.474

[a] Ewald parameters for MM (reference 88): Coulombic: $d = 1 \times 10^{-6}$ kcal/mol, $h_{opt} = 2.135$ Å, $R_{cut} = 9.070$ Å, $H_{cut} = 0.724$ Å^{-1}; Attractive vdW: $d = 1\times10^{-6}$ kcal/mol, $h_{opt} = 3.430$ Å, $R_{cut} = 12.700$ Å, $H_{cut} = 0.400$ Å^{-1}; Repulsive vdW: $R_{cut} = 9.120$ Å. [b] Ewald parameters for MD (reference 88): Coulombic: $d = 1 \times 10^{-3}$ kcal/mol, $h_{opt} = 2.191$ Å, $R_{cut} = 7.400$ Å, $H_{cut} = 0.588$ Å^{-1}; Attractive vdW: $d = 1 \times 10^{-2}$ kcal/mol, $h_{opt} = 3.830$ Å, $R_{cut} = 8.300$ Å, $H_{cut} = 0.220$ Å^{-1}; Repulsive vdW: $R_{cut} = 5.360$ Å. [c] References 38 and 39.

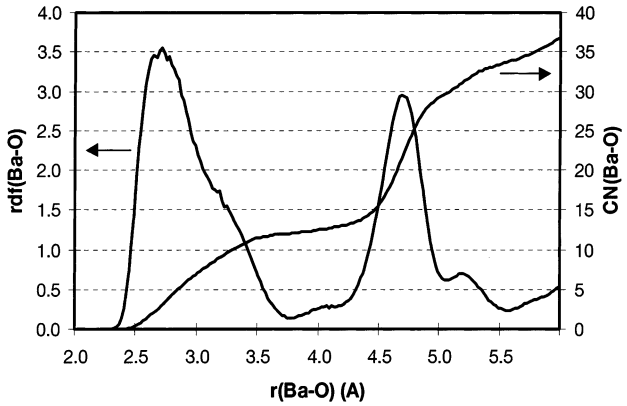

Figure 3. Ba−O radial distribution function (RDF) and the total coordination number (CN) of O around a Ba as a function of distances, which show that the first nearest-neighbor shell includes 12 oxygen atoms around one barium at distances of 2.5−3.5 Å.

4.1. Density and Structure. With the final FF parameters, we calculate a density for $BaSO_4$ as 4.473 ± 0.003 g/cm^3 from the MD simulation at 298 K, in excellent agreement with the experimental density[39] of 4.474 g/cm^3. The calculated lattice parameters at 298 K differ by 1−4% from experiment (Table 9). Figure 3 shows the radial distribution function (RDF) and the integrated coordination number (CN) of oxygen atoms around a barium atom. It shows a CN of 12 and an average distance of 2.7∼3.3 Å for oxygens in the first nearest-neighbor shell around a barium in agreement with experiment (section 2.1).[38,39] Figure 4 shows some detail of the structure.

4.2. Energetics. The thermodynamic lattice energy (in fact, enthalpy) of $BaSO_4$ at 298 K was calculated using eq 9:

$$\Delta H_{\mathrm{latt,298K}} = \Delta H^0_{\mathrm{f,298K}}(\mathrm{BaSO_4(cr)}) - \Delta H^0_{\mathrm{f,298K}}(\mathrm{Ba^{2+}(g)}) - \Delta H^0_{\mathrm{f,298K}}(\mathrm{SO_4^{2-}(g)}) \quad (9)$$

where the enthalpy of each state at 298 K was calculated by

$$\Delta H^0_{\mathrm{f,298K}} = E_{\mathrm{MM,0K}} + \mathrm{ZPE} + \Delta H_{0\rightarrow 298\mathrm{K}} \quad (10)$$

and $E_{MM,0K}$ denotes the energy at 0 K obtained from minimization. The zero-point energy (ZPE) and thermodynamic properties at various temperatures were calculated from the vibrational frequencies of the minimized structure of $BaSO_4$ using a 5 × 5 × 5 grid of points in the Brillouin zone[89] (using *PolyGraf* software[90]). With the final FF, eq 9 led to a lattice energy of 592.97 kcal/mol (Table 10).

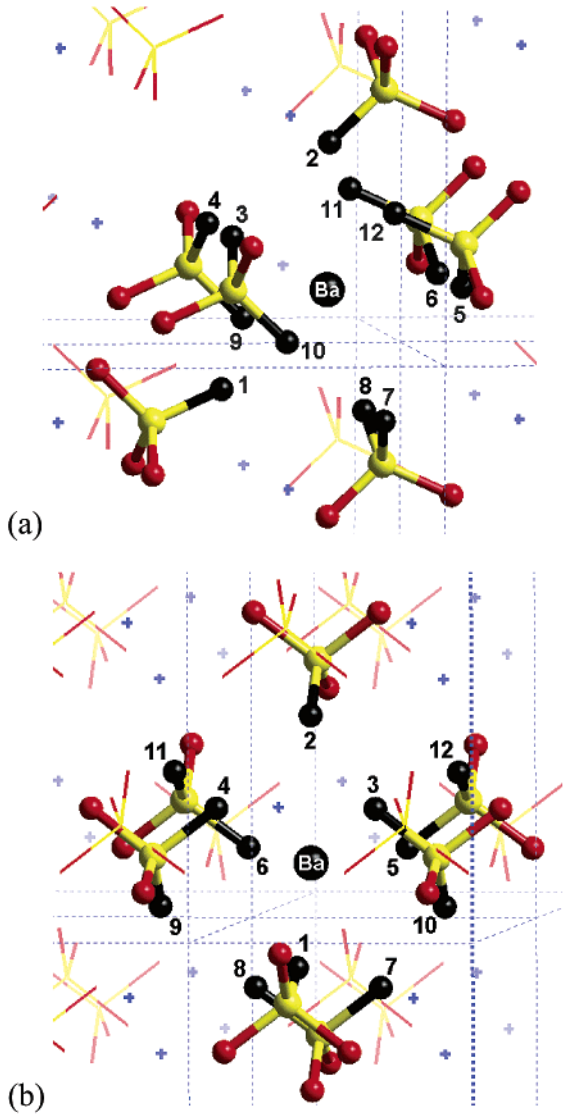

Figure 4. Nearest-neighbor oxygens around a barium ion viewed along (a) the [010] direction and (b) the [100] direction. The Ba−O distances are 2.77 (O1), 2.81 (O2), 2.82 (O3−6), 2.86 (O7−8), 3.08 (O9−10), and 3.32 Å (O11−12).

The lattice energy of $BaSO_4$ at 298 K was also calculated by assuming

$$\Delta H^0_{\mathrm{f,298K}} = \langle \mathrm{PE} \rangle_{\mathrm{MD,298K}} \quad (11)$$

where $\langle PE\rangle_{MD,298K}$ denotes the average potential energy obtained from the MD simulation at 298 K. Equation 11 led to a lattice energy of 591.6 kcal/mol (Table 10). These values agree well with experimental data of 592.3 kcal/mol (section 2.2).

4.3. Compressibility. The elastic constants and compressibility of $BaSO_4$ were calculated using various methods (Table 11). The second derivative method at the optimal structure at 0 K is the faster calculation. However, this cannot be compared directly with experiment, which is usually performed at room temperature. Consequently, we calculated the compressibility from NPT MD simulations at 298 K. One approach is to use the relationship between compressibility and volume fluctuation over the MD trajectory

$$\chi = \frac{1}{\bar{V}RT}\langle V^2 - \bar{V}^2 \rangle \quad (12)$$

TABLE 10: Lattice Enthalpy (or Lattice Energy; kcal/mol) Per Formula Unit of $BaSO_4$ at 298 K

	MM (0 K) with corrections to 298 K				MD (298 K)	
	$E_{MM,0K}$	ZPE	$\Delta H_{0\rightarrow 298K}$	$\Delta H^0_{f,298K}$	⟨PE⟩	expt (298 K)
$BaSO_4$	−593.60	11.7600	4.5679	−577.27	−588.1 ± 0.1	
SO_4^{2-}	0	9.945	4.2717	14.217	2.6143 ± 0.0002	
Ba^{2+}	0	0	1.48[a]	1.48	0.888[b]	
$\Delta H_{latt,298K}$				592.97	591.6	592.3[c]

[a] 2.5 *RT*. [b] 1.5 *RT*. [c] See Table 3.

TABLE 11: Compressibility χ (GPa^{-1}) Calculated with Various Methods

	2nd derivative	MDs at 298 K and −0.5 to +0.5 GPa		MD at 298 K and 0.0001 GPa[d]		
method	(0 K)	linear fit	4th order fit	adiabatic	isothermal	expt
χ	0.01802[a]	0.01767[b]	0.01936[c]	0.02463[d]	0.02488[d]	0.0170−0.0192[e]

[a] From the second derivative of energy with respect to volume at 0 K. [b] From the linear fit of the ⟨*P*⟩−⟨*V*⟩ plot. [c] From the fourth-order fit of the ⟨*P*⟩−⟨*V*⟩ plot. [d] From the fluctuation of volume during final 250 ps out of 300-ps MD at 298 K. [e] See Table 4.

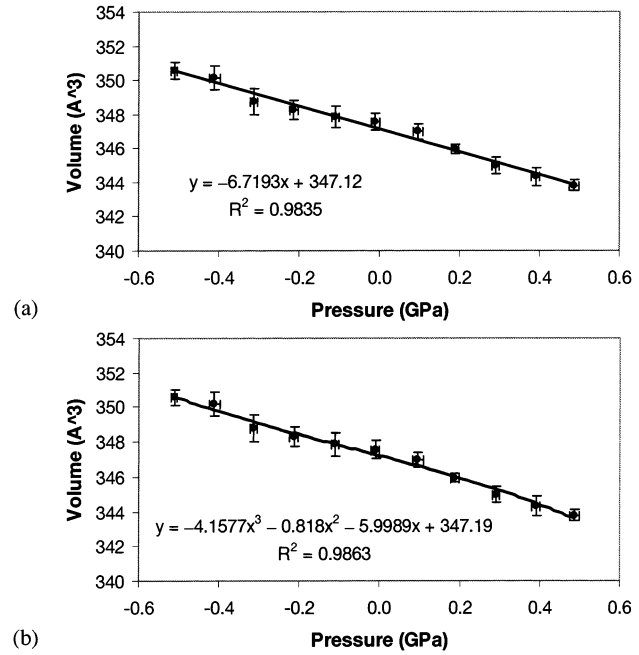

Figure 5. ⟨*P*⟩−⟨*V*⟩ curve used to estimate compressibility from its slope at $P = 0$. ⟨*P*⟩ and ⟨*V*⟩ are the average values during a 350-ps MD simulation after a 50-ps equilibration. The errors were estimated from the standard deviation between 14 block-averages during each 25-ps block. The slope was taken from (a) the first-order (linear) fit and (b) the fourth-order fit.

However, we found that this approach requires very long simulation time to obtain a reliable converged value. Consequently, we performed MD simulations for 298 K at eleven different pressures ranging from −0.5 to 0.5 GPa (−5000 to 5000 bar) and at each point obtained the average volume and average pressure for 350 ps following a 50-ps equilibration. The ⟨*P*⟩−⟨*V*⟩ curve is shown in Figure 5. Using eq 6 we calculated the compressibility at 298 K from the slope of the ⟨*P*⟩−⟨*V*⟩ over *V* at $P = 0.0001$ GPa (1 bar). Assuming a linear (first-order) fit leads to $\chi = 0.0177$ GPa^{-1}, whereas using a fourth-order fit leads to 0.0194 GPa^{-1}, respectively. The experimental compressibility ranges from 0.0170 to 0.0192 GPa^{-1} (section 2.3) in good agreement with our values obtained from ⟨*P*⟩−⟨*V*⟩.

4.4. Vibrational Frequency. The vibrational frequencies of SO_4^{2-} were calculated at the minimized structure (0 K). As shown in Table 12 they are in good agreement with experiment (section 2.4): the symmetric stretch (ν_1) is at 986 cm^{-1} for both theory and experiment, whereas the asymmetric stretch (ν_3) is within 3 cm^{-1} of experiment. The angle bends (ν_2, ν_4) are also within 3 cm^{-1} of experiment. This indicates that the SO_4 valence forces are accurately described.

TABLE 12: Frequencies (cm^{-1}) of Internal Modes of $BaSO_4$ Crystal (Four SO_4 Per Unit Cell)

	Raman	IR
	Calculations	
ν_1 (*A*)	986	986, 980
ν_2 (*E*)	461, 460, 453, 451	
ν_3 (T_2)	avg. 1122	avg. 1122
ν_4 (T_2)	avg. 627	avg. 612
	Experiment	
ν_1 (*A*)	986[b]	985, 984[b]
ν_2 (*E*)	462, 461, 453, 451[b]	
ν_3 (T_2)	avg. 1125[b]	avg. 1107,[b] 1121[c]
ν_4 (T_2)	avg. 627[b]	avg. 615[b]

[a] The frequencies were calculated at the Γ point of the Brillouin zone. [b] References 66 and 67. [c] Reference 68.

5. Force Field for Water: F3C

For water, we used the F3C FF of Levitt and co-workers.[91] The parameters of this FF are shown in Table 13. This flexible three-centered (F3C) water FF had been designed for use in simulations of macromolecules in solution and developed to have the same potential form as used for the solutes: (1) it uses only the atoms as interaction centers (without any additional interaction centers such as lone pairs), (2) it does not fix bond lengths nor bond angles, and (3) in particular it includes vdW interactions with the hydrogen atoms, whereas other widely used water potentials (Stillinger-Rahman,[92,93] SPC,[94,95] TIP3P,[95,96] TIP4P,[95] and SPC/E[95,97]) use vdW interactions that act only between the oxygen atoms. We were concerned that a lack of H vdW might cause problems in describing the interaction between water with Ba and SO_4. The F3C FF was shown to give water properties (potential energy, heat capacity, diffusion constant, and RDFs) in reasonable agreement with experiments.[91]

Because the simulation conditions employed in this original F3C work[91] (NVE MD with the minimum image conventions with a smooth truncation function) are different from those employed in the current study (NPT MD with the Ewald method), the quality of the F3C FF in combination with these new conditions was first demonstrated by calculating the density, potential energy, and RDFs (O−O and O−H) of a water bath containing 267 water molecules after 200-ps NVT and NPT MD simulations at 298 K with the Ewald method. The calculated properties are in good agreement with experiments. The detailed results are given in Appendix B.

TABLE 13: Force Field Parameters for Water, Ba−Water, and SO_4−Water

water[a]	$E^{coulomb}$	$q(O_w)$	−0.820|e|				
		$q(H_w)$	0.410|e|				
	E^{vdW} [b]	$R_o(O_w)$	3.5532[c]	$D_o(O_w)$[d]	0.1848		
		$R_o(H_w)$	0.9000[c]	$D_o(H_w)$[d]	0.01		
	E^{bond}(OH)	R_o	1.000[c]	K_b[e]	250		
	E^{angle}(HOH)	θ_o	109.47[f]	K_θ[d]	60		
water−$BaSO_4$	E^{vdW} [g]	$R_o(O_w)$	3.5532[c]	$D_o(O_w)$[d]	0.1848	$\zeta(O_w)$	13.000
		$R_o(H_w)$	3.195[c]	$D_o(H_w)$[d]	0.0123	$\zeta(H_w)$	12.382

[a] Reference 91. [b] Lennard-Jones potential. [c] In Å. [d] In kcal/mol. [e] In kcal/mol/Å^2. [f] In degrees. [g] For functional forms, see Table 6.

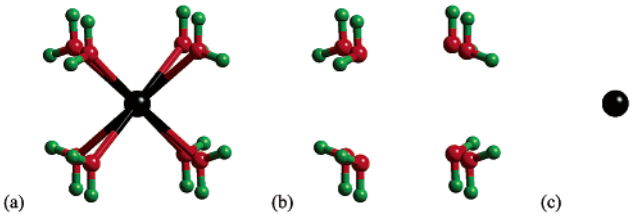

Figure 6. Model describing the Ba^{2+}−H_2O interaction: (a) $Ba(H_2O)_8^{2+}$, (b) $(H_2O)_8$, and (c) Ba^{2+}.

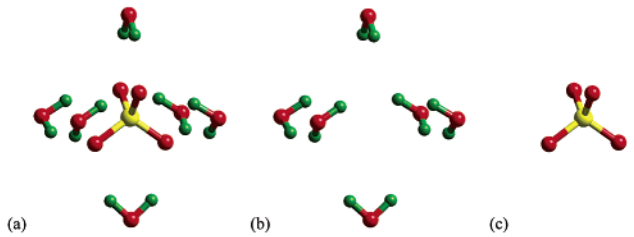

Figure 7. Model describing the SO_4^{2-}−H_2O interaction: (a) $(SO_4)(H_2O)_6^{2-}$, (b) $(H_2O)_6$, and (c) SO_4^{2-}.

6. Ba−Water and SO_4−Water Interaction Modeled by $Ba(H_2O)_8^{2+}$ and $(SO_4)(H_2O)_6^{2-}$ Clusters

To determine the interaction of water with Ba^{2+} and SO_4^{2-}, we performed ab initio QM calculations on water clusters of Ba^{2+} and SO_4^{2-} and fit the FF parameter to reproduce the resulting binding energy and structure. According to X-ray diffraction (XRD) studies, the nearest-neighbor shell of Ba^{2+} in water is composed of about 9.5 water molecules (Ba−O_w distance at 2.9 Å)[98−100], and a sulfate unit (SO_4^{2-}) is surrounded by a nearest-neighbor shell of 6−14 waters with the S−O_w distance at 3.7−3.9 Å.[98,99] We chose the most symmetric configuration of water clusters with the minimum number of water molecules in these ranges: $Ba(H_2O)_8^{2+}(D_{4h})$ and $(SO_4)(H_2O)_6^{2-}$ (Figures 6a and 7a).

The QM calculations were done at the B3LYP/LACVP* or LMP2/LACVP* level (the LACVP* basis set uses 6-31G* for S and O and the Hay−Wadt effective core potential and basis set for Ba). Basis set superposition error (BSSE) was corrected by counterpoise (CP) method. All of these calculations used *Jaguar*.[76] The binding energy (BE) is defined as in Figures 6 and 7:

$$\mathrm{BE[Ba{-}water]} = E[Ba^{2+}] + E[(H_2O)_8] - E[Ba(H_2O)_8^{2+}] \quad (13)$$

$$\mathrm{BE[SO_4{-}water]} = E[SO_4^{2-}] + E[(H_2O)_6] - E[(SO_4)(H_2O)_6^{2-}] \quad (14)$$

where $(H_2O)_8$ is in the same configuration as in $Ba(H_2O)_8^{2+}$ and $(H_2O)_6$ is in the same configuration as in $(SO_4)(H_2O)_6^{2-}$. This is called the *snap* binding energy. By using this definition, we can separate out the pure Ba−water or sulfate−water interaction from the interaction between waters. The snap binding energy and structural parameters are listed in Tables 14 and 15.

TABLE 14: QM and FF Calculations for $Ba(H_2O)_8^{2+}$

	QM (B3LYP/LACVP*)		
	before CP	after CP	FF
snap BE[a]	252.8	248.3	252.1
optimum r(Ba−O_w) (Å)	2.88		2.92

[a] Snap binding energy (in kcal/mol) = $E[Ba^{2+}] + E[(H_2O)_8] - E[Ba(H_2O)_8^{2+}]$ where $(H_2O)_8$ is in the same configuration as in $Ba(H_2O)_8^{2+}$.

TABLE 15: QM and FF Calculations for $(SO_4)(H_2O)_6^{2-}$

	QM (B3LYP/6-31G*)		QM(LMP2)	
	before CP	after CP	before CP	FF
snap BE[a]	183.2	146.7	175.8	170.3
r(S−O_w) (Å)	3.49			3.42
r(O−O_w) (Å)	2.90			2.83
r(S−H_w) (Å)	2.94			2.88
r(O−H_w) (Å)	2.03			1.95

[a] Snap binding energy (in kcal/mol) = $E[SO_4^{2-}] + E[(H_2O)_6] - E[(SO_4)(H_2O)_6^{2-}]$ where $(H_2O)_6$ is in the same configuration as in $(SO_4)(H_2O)_6^{2-}$.

The large difference between the B3LYP values with and without the BSSE indicates that the 6-31G* basis set might be inadequate to study the SO_4^{2-}−H_2O interactions. Thus, we also used a larger basis set (6-31G**++) to calculate the structures and snap binding energies of these clusters and found this gives similar results with or without the CP correction (section 7.3).

The "off-diagonal" nonbonding FF used for the Ba−water and sulfate−water interaction (Table 13) has the same form as used for $BaSO_4$ (Table 6). The same combination rule [eq 8] is used to combine the vdW parameters of $BaSO_4$ (three-parameter exponential-6 FF) and of water (two-parameter LJ 12 FF) to produce the off-diagonal vdW parameters (three-parameter exponential-6 FF). The R_o and D_o values of the LJ 12−6 potential of water oxygen (O_w) were taken for the combination, and the ζ value of O_w was optimized to reproduce the QM binding energy and structure of the $Ba(H_2O)_8^{2+}$ cluster. For H_w, we borrowed the potential from Dreiding[71] rather than from the water potential and slightly changed the parameters to reproduce the SO_4−water interaction. The comparison between ab initio results and the values obtained from optimizing the structure using the final FF (Table 13) is listed in Tables 14 and 15. (An alternative FF was also developed to fit to the results calculated with the 6-31G**++ basis set, as shown in section 7.3.)

7. Surface Energy (Surface Tension)

7.1. Solid−Vacuum Interface. To model the barite−vacuum interface, we cleaved the crystal for each of low-index surfaces to form a two-dimensional infinite slab of finite thickness. The calculation describes this as a 3D system in which a layer of vacuum separates each slab. The 2 × 2 × 2 $BaSO_4$ layer was

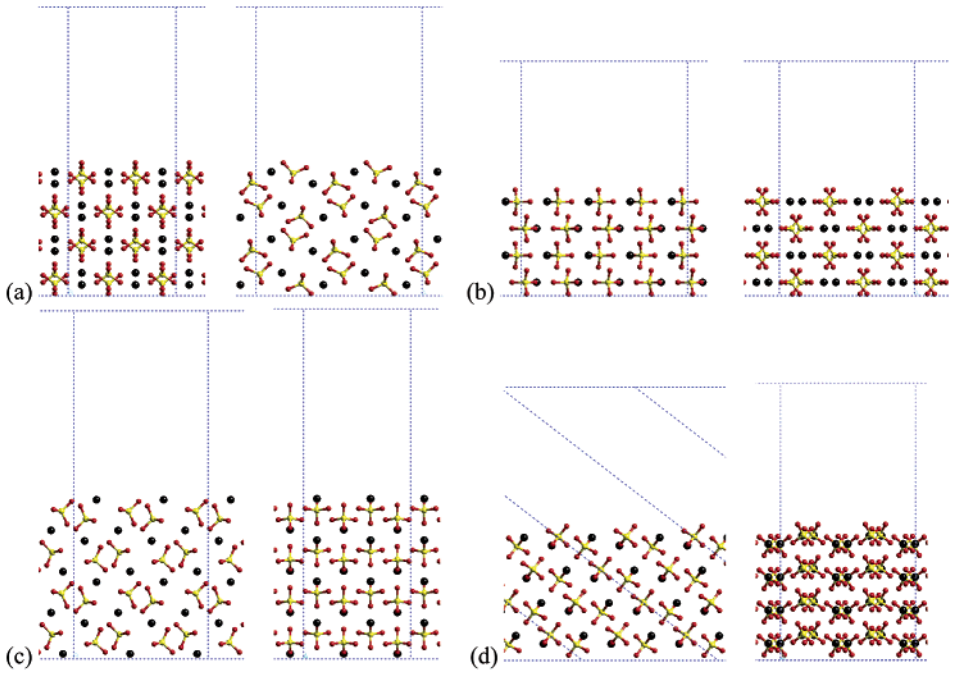

Figure 8. Model of the barite−vacuum interface viewed along [100] (left) and [010] directions (right). (a) (001), (b) (010), (c) (100), and (d) (210).

TABLE 16: Calculated Surface Energies for Barite−Vacuum Interfaces

(a) FF without relaxation	(210)	(001)	(010)	(100)
E(slab) (kcal/mol)[a]	−18536.7	−18563.5	−18315.7	−18400.8
$\Delta E/2$ (kcal/mol)[a]	229.5	216.2	340.0	297.5
surface area (Å^2)	199.51	194.43	243.89	157.91
surface energy (mJ/m^2)	799.4	772.4	968.7	1309
(b) FF with relaxation (MM)	(210)	(001)	(010)	(100)
E(slab) (kcal/mol)[a]	−18695.4	−18600.6	−18480.7	−18586.1
$\Delta E/2$ (kcal/mol)[a]	150.2	197.6	257.5	204.9
surface area (Å^2)	199.51	194.43	243.89	157.91
surface energy (mJ/m^2)	523.1	706.1	733.7	901.3
RMS deviation from bulk (Å)	0.386	0.086	0.389	0.221
(c) NVT MD at 298 K[b]	(210)	(001)	(010)	(100)
E(slab) (kcal/mol)[c]	−18524.9 ± 0.2	−18478.5 ± 0.9	−18311.7 ± 0.3	−18420.6 ± 1.2
$\Delta E/2$ (kcal/mol)[c]	149.2 ± 0.2	172.4 ± 0.5	255.8 ± 0.3	201.3 ± 0.6
surface area (Å^2)	199.51	194.43	243.89	157.91
surface energy (mJ/m^2)	519.5	616.0	728.7	885.8
RMS deviation from bulk (Å)	0.45 ± 0.02	0.37 ± 0.02	0.49 ± 0.06	0.82 ± 0.07
change in surface energy (mJ/m^2)[d]	−279.9	−156.4	−240.0	−423.2

[a] E(reference system) = E(barite bulk) = −18995.8 kcal/mol. [b] From the last 70 ps out of an 80-ps trajectory. [c] E(reference system) = E(barite bulk) = −18823.3 ± 0.4 kcal/mol. [d] Change in surface energy = surface energy in (c) − surface energy in (a).

used to model an 11−17 Å barite slab separated by a 40-Å layer of vacuum. The unit cell has 32 $BaSO_4$ units or 192 atoms. The various structures are shown in Figure 8.

The surface energy (per unit area, that is, the surface tension) is defined as

$$E_{\text{surface}}^{\text{barite-vacuum}} = \frac{1}{2}\frac{E(\text{barite slab}) - E(\text{barite bulk})}{\text{surface area}} \quad (15)$$

Three types of surface energies were calculated (Table 16): (a) surface creation energy without relaxation, (b) surface energy with relaxation at 0 K by minimization (MM), and (c) surface energy with relaxation at 298 K by MD simulation.

The surface generation, without any relaxation, causes the loss of nearest-neighbor oxygens around each surface barium atom. Figure 9 shows how the average coordination number of oxygen atoms around a single surface barium atom changes with distance. On the basis of the coordination number up to 3.7 Å, we conclude that cleavage at (001) results in losing 2 nearest-neighbor oxygens around each surface barium (from 12 to 10), and a loss of 2.5 (from 12 to 9.5) results after cleavage at the (210) and (100) surfaces. The cleavage at the (010) surface results in losing 4 nearest-neighbor oxygens (from 12 to 8).

This is correlated with the energy cost to generate the surface with the same number (8) of surface barium atoms (which is not divided by the surface area):

216 for (001) < 230 for (210) < 298 for (100) < 340 for (010)

(in kcal/mol; Table 16a). However, the large surface area of the (010) surface places this surface low in the surface energy after dividing by the surface area:

772 for (001) < 799 for (210) < 969 for (010) < 1309 for (100)

(in mJ/m^2; Table 16a).

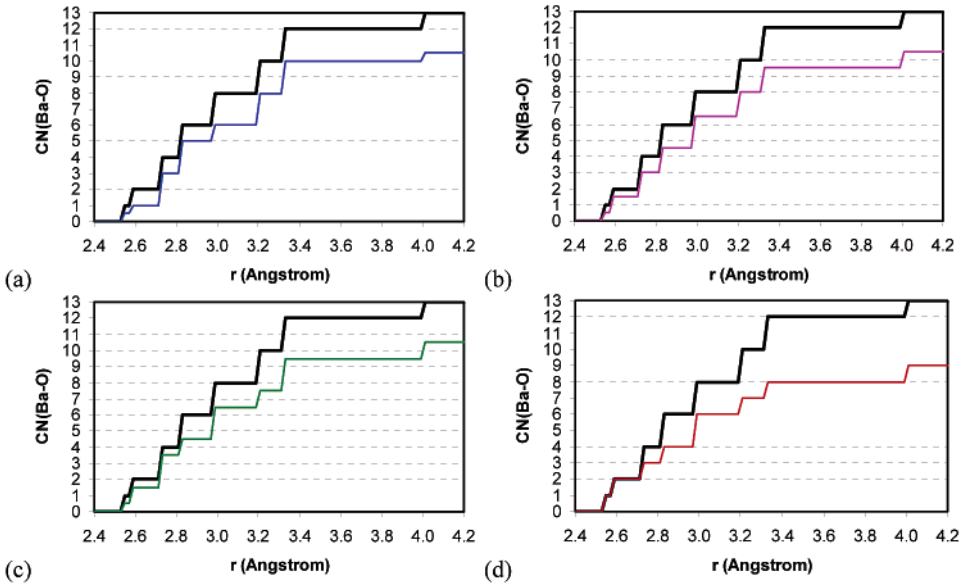

Figure 9. Coordination number of oxygens around a surface barium of various non-relaxed barite surfaces as a function of distance. (a) (001), (b) (210), (c) (100), and (d) (010). The corresponding coordination number in the bulk barite is shown in thick line for comparison. The atoms within 3.7 Å were considered as nearest-neighbors. The figure shows that a barium on the (001) surface has 10 nearest-neighbor oxygens around it on average, 9.5 on (210) and (100), and 8 on (010).

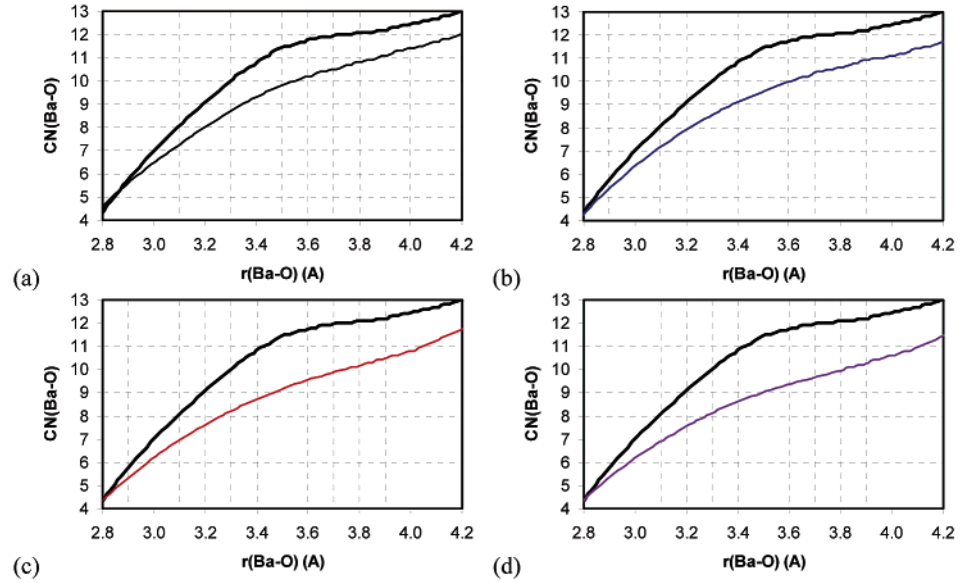

Figure 10. Coordination number of oxygens around a surface barium of various relaxed (by MD) barite surfaces as a function of distance. (a) (001), (b) (210), (c) (100), and (d) (010). The corresponding coordination number in the bulk barite is shown in a thick line for comparison. The atoms within 3.7 Å were considered as nearest-neighbors. The figure shows that a barium on the (001) and (210) surfaces has 10.5 nearest-neighbor oxygens around it on average, whereas the one on (100) has 10, and the one on (010) has 9.5.

The relaxation leads to a reorientation of sulfate group and/or a reposition of the barium atom to make up the loss of the attractive Ba−O interaction.

Figure 10 shows the average coordination number of oxygen atoms around a single surface barium atom as a function of distance, which was calculated from the MD. On the basis of the coordination number up to 3.7 Å, the cleavage at (001) and (210) results in the coordination of 10.5 oxygens around each surface barium. This corresponds to a loss of 1.5 oxygens when compared with the bulk. This also corresponds to a recovery of 0.5 and 1.0 lost oxygens when compared with the non-relaxed (001) and (210), respectively. The cleavage at the (100) surface results in the coordination of 10 oxygens around each surface barium, corresponding to a loss of 2 oxygens compared with the bulk and a recovery of 0.5 lost oxygens compared with the non-relaxed (100). The cleavage at the (010) surface results in the coordination of 9.5 oxygens around each surface barium, corresponding to a loss of 2.5 oxygens compared with the bulk and a recovery of 1.5 lost oxygens compared with the non-relaxed (010).

From this result, we can expect that the surface energy is reduced in a great deal with the relaxation and that the surface energies of (210) and (001) are lower with respect to (100) and (010).

Indeed, the MD (Table 16c) and MM (Table 16b) calculations agree with each other in the sequence of surface energy

$$(210) < (001) < (010) < (100)$$

and in the significantly reduced value of surface energy of each surface [$\sim$520 mJ/m^2 (=520 dyn/cm) for (210), $\sim$730 mJ/m^2

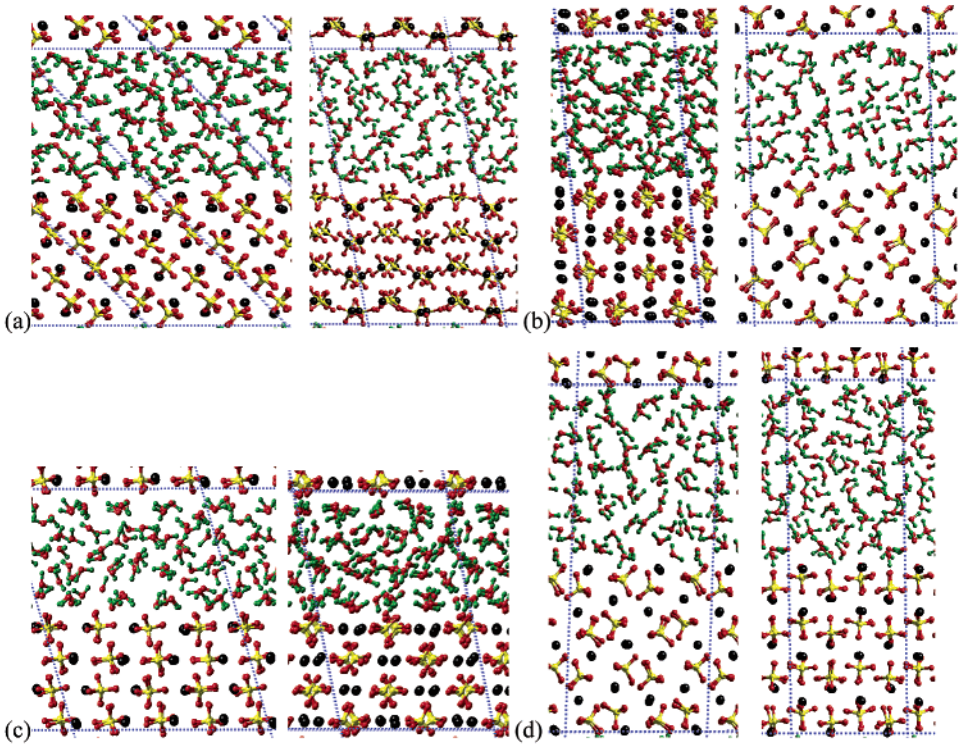

Figure 11. Barite−water interfaces viewed along the [100] (left) and [010] directions (right). Snapshots after 80 ps of MD simulations. (a) (210), (b) (001), (c) (010), and (d) (100).

for (010), and ~900 mJ/m^2 for (100) from both calculations] except the (001) surface. The MD indicates that the surface energy of (001) (616 mJ/m^2) is significantly lower than ~730 mJ/m^2 of (010), whereas the MM puts (001) (706 mJ/m^2) and (010) very similar. The MM seems to place the surface energy of (001) too high. As a measure of the structural relaxation during the MD and the MM, we calculated the RMS (root-mean-square) differences in atomic positions between the relaxed structure and the bulk crystal structure (Table 16b,c). For (001), the MM leads to an RMS change as small as 0.08 Å, whereas the MD leads to a change of 0.37 Å. The other surfaces relax by 0.22−0.39 Å during MM. These indicate that the (001) surface does not relax enough with minimization alone and that the MM places the surface energy of (001) too high. The MD seems to lead to enough relaxation for the (001) surface [the RMS change of 0.37 Å for (001) and 0.45, 0.49, and 0.82 Å for other surfaces].

The final sequence and the value of the surface energies calculated from the MD calculation are similar to those reported in the previous calculations.[30] The (210) surface has the lowest surface energy followed by (001), indicating that these two surfaces are the most stable intrinsically.

Another interesting sequence is based on the amount of relaxation in the structure and in the energy after the surface generation. The RMS changes in atomic positions after the MD are in the sequence of

$$0.37 \text{ for } (001) < 0.45 \text{ for } (210) < 0.49 \text{ for } (010) < 0.82 \text{ for } (100)$$

(in Å; Table 16c). The reduction in the surface creation energy cost (not divided by the surface area) with the MD is in the sequence of

$$44 \text{ for } (001) < 80 \text{ for } (210) < 84 \text{ for } (010) < 96 \text{ for } (100)$$

(in kcal/mol; Table 16a,c). The recovery of lost oxygens (Figures 9 and 10) is in sequence of

$$0.5 \text{ for } (001), (100) < 1.0 \text{ for } (210) < 1.5 \text{ for } (010)$$

Overall, the (001) surface has the smallest amount of change (relaxation) since its generation. This might be relevant with the fact that the (001) surface is the only surface that can be cut clean and stable.[15,16,101]

7.2. Solid−Water Interface. To investigate the effect of water solvent on surface energy, we use the same $BaSO_4$ slab as above but replaced the vacuum layer with water (Figure 11). This was initialized by immersing the system into an equilibrated water bath. We carried out NPT MD simulations on this composite system and also on bulk water to estimate the energy of reference system. The barite−water surface energy was defined as

$$E_{\text{surface}}^{\text{barite-water}} = \frac{1}{2}\frac{E(\text{composite}) - E(\text{BaSO}_4(\text{bulk})) - E(\text{water(bulk)})}{\text{surface area}} \quad (16)$$

To determine the dependence of the results on the number of $BaSO_4$ layers and on the height of water bath (i.e., separation between $BaSO_4$ blocks), we examined the (010) surface (which has the shortest value of the separation in the z direction both between $BaSO_4$ layers and between $BaSO_4$ blocks) and increased the number of $BaSO_4$ layers ($2 \times 2 \times 3$; 6 layers) and the height of water bath (19 Å with 139 water molecules compared to 11 Å with 91 water molecules), and then we compared the surface energy with that from smaller system. The results in Table 17 show that the surface energies for these two cases are similar (262 ± 12 and 265 ± 14 mJ/m^2). Thus, for the comparison between various surfaces, we chose $2 \times 2 \times 2$ $BaSO_4$ layers in

TABLE 17: Convergence Test for the (010) Surface Energies with Respect to the Thickness of Barite Slab and Water Bath[a]

	2×2×2 with 91 water	2×2×3 with 139 water
E(composite) (kcal/mol)	−19567 ± 6	−29467 ± 4
E(bulk barite)	−18823.3 ± 0.4	−28234.9 ± 0.6
E(bulk water)	−930 ± 6	−1420 ± 9
$\Delta E/2$ (kcal/mol)	93 ± 4	94 ± 5
surface area (Å^2)	246.7 ± 0.2	246.2 ± 0.2
surface energy (mJ/m^2)	262 ± 12	265 ± 14

[a] Calculated surface energy for barite−water interface from 100-ps MD simulation at 298 K.

TABLE 18: Calculated Surface Energies for the Barite−Water Interfaces from 100-ps MD Simulations at 298 K

surface	(210)	(001)	(010)	(100)
E(composite)[a] (kcal/mol)	−19598 ± 3	−19574 ± 6	−19567 ± 6	−19568 ± 5
$\Delta E/2$[a] (kcal/mol)	78 ± 3	90 ± 6	93 ± 4	93 ± 4
surface area (Å^2)	198.9 ± 0.2	194.8 ± 0.2	246.7 ± 0.2	160.3 ± 0.2
surface energy (mJ/m^2)	271 ± 12	319 ± 23	262 ± 12	402 ± 16
change from vacuum case (mJ/m^2)	−172	−201	−324	−336

[a] E(bulk water) = −930 ± 6 kcal/mol. E(bulk barite) = −18823.3 ± 0.4 kcal/mol. E(reference system) = E(bulk water) + E(bulk barite) = −19753 ± 6 kcal/mol.

contact with an 11-Å-thick water bath including 91 water molecules.

The barite−water surface energy (Table 18) is much lower than barite−vacuum surface energy because the water layer near the surface arranges to interact favorably with the barite surface replacing the missing neighbors in the solid−vacuum case. The (100) and (010) surfaces which were less stable at the vacuum interface (because of more missing neighbors) are stabilized to a larger extent by the interaction with water. Thus, the variation between different surfaces is much smaller in the barite−water case than for the barite−vacuum case.

The calculated surface energies in Table 18 are in the sequence of

$$(010) \sim (210) < (001) \ll (100)$$

The (210) and (010) surfaces are indicated to have smaller surface energies (271 ± 12 and 262 ± 12 mJ/m^2), whereas (001) is much higher (319 ± 24 mJ/m^2), and (100) is even higher (402 ± 16 mJ/m^2). Because barite crystals are precipitated from aqueous solution, it is these values that should be compared to surface energies of crystals. However, the morphological data summarized in Table 19,[29] if they are directly related to the surface energies, indicate the experimental surfaces energies in the sequence of

$$(001) \sim (210) < (010) < (100)$$

The (210) and (001) surfaces are the ones found the most often from the morphology study of barite in aqueous environment.[11,22,29] No experimental evidence has been found for the dominant presence of the (010) surface in aqueous solution. This indicates that the calculations estimate the (010) surface too stable and the (001) surface too unstable. Also, the calculation

TABLE 19: Statistical Data on the Morphology of Barite[a]

form	P[b]	F[c]	H[d]	G[e]
{210}	91.9	91.3	84.7	66.8
{002}	97.8	94.8	88.4	83.3
{020}	70.8	54.0	38.8	23.8
{200}	61.1	50.0	31.9	14.1

[a] Reference 29. [b] P = Percentage of different combinations of forms in which the form occurs. [c] F = Percentage of geographically different deposits in which the form has been observed. [d] H = Percentage of times the form has been recorded. [e] G = Relative largeness of the face using a weight factor 3 for large, 2 for intermediate, and 1 for small faces.

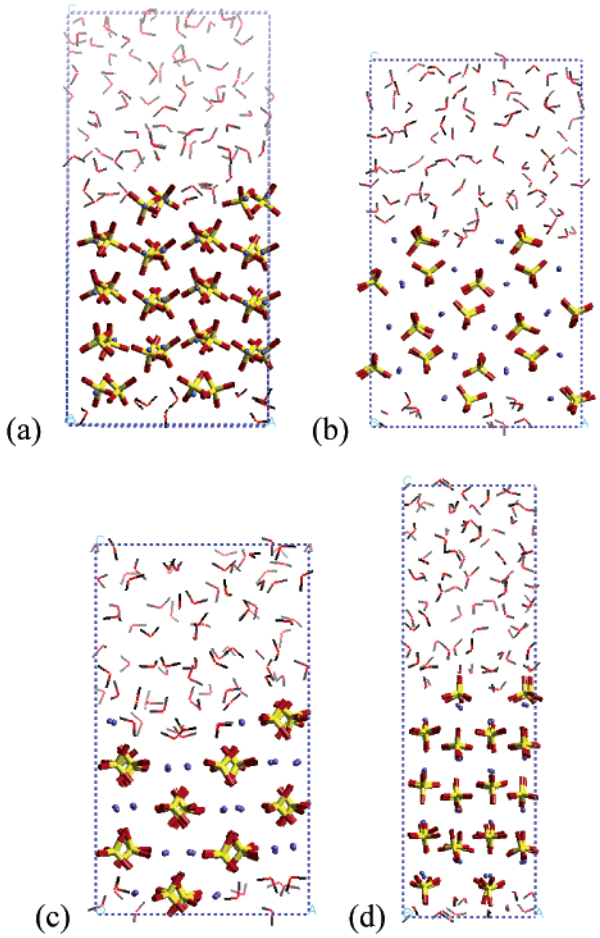

Figure 12. Half-monolayer barite−water interfaces viewed along the [010] direction. (a) (210), (b) (001), (c) (010), and (d) (100) surfaces.

does not reproduce clearly the relative stabilities of (210), (001), and (010) surfaces. However, both calculation and experiment agree that the (100) surface is least stable.

One possible reason for this discrepancy could be that the surface energy is not an exclusive factor to determine the morphology of crystals. The crystal growth rate in the direction of each surface normal, which is closely related to the morphology, is a kinetic property, whereas the surface energy is a thermodynamic one.

Thus, as a very crude and qualitative measure of the kinetics of the crystal growth in the direction of each surface normal, we made the top and the bottom layers of each surface as half-monolayers (Figure 12) in order to represent the midpoint of the layer-by-layer growth of the surface and submitted it to NPT MD simulations (Table 20). Higher surface energy change from the monolayer surface would indicate how difficult to make half-monolayers, that is, how slow the growth would be. This

TABLE 20: Calculated Surface Energies (mJ/m^2) of Barite−Water Interfaces with Half-Monolayers

surface	(210)	(001)	(010)	(100)
surface energy (half-monolayer)	313 ± 15	392 ± 17	321 ± 13	384 ± 16
surface energy (monolayer)	271 ± 12	319 ± 23	262 ± 12	402 ± 16
change from monolayer	41 ± 19	65 ± 29	59 ± 18	−17 ± 23

factor shows that surfaces would grow slowly in the sequence of

$$(001) \sim (010) \sim (210) \ll (100)$$

Indeed, this is in closer agreement with experiments, with the only exception being the reversed order of (010) and (210). Thus, the difficulty in making half-monolayers for the (001) surface explains the slow growth rate of (001) observed experimentally. A combination of concepts from surface energy and surface growth might be important in explaining crystal morphology.

Our simulation results assume fully deprotonated sulfate surfaces and assume a high pH, whereas the experiment was based on the observations in the range of temperature between 25 and 75 °C and of pH between 3 and 7.[22] This might also contribute to the discrepancy between our calculational surface energy and the experimental surface area.

7.3. Solid−Water Interface Re-examined with Another FF. The exaggerated stability of the (010) surface in the calculation and the largest surface area of the (010) surface seem to imply another possible reason for the discrepancy. It is possible that the FF for the $BaSO_4$−water interaction used in our simulation is too attractive even though we calibrated it with QM calculations on Ba−water and SO_4−water clusters (section 6). This is because the definition of the binding energy from QM (particularly with a small basis set) is ambiguous because of the BSSE and the FF was fit to the higher end of the binding energy (Tables 14 and 15). Thus, we explored this possibility by repeating the same calculations on those barite−water interfaces with an alternative, less attractive FF ($\zeta(O_w) = 14.4$ instead of 13.0, $\zeta(H_w) = 8.6$ instead of 12.382, and $D_o(H_w) = 0.0152$ kcal/mol instead of 0.0123 kcal/mol), which developed to fit to QM results obtained with a higher basis set (6-31G**++ for S, O, and H; Tables 21 and 22). This leads to higher surface energies for all surfaces in contact with water (Table 23). However, the sequence of relative surface energies[(210) ∼ (010) < (001) ≪ (100)] is still similar to the one obtained with the 6-31G*-based FF.

8. Summary

This work determined a FF for the $BaSO_4$ crystal in contact with water. This MSXX FF reproduces the experimental density (4.473 g/cm^3 from MD and 4.474 g/cm^3 from experiments at 298 K), lattice energy (591.6−593.0 kcal/mol from calculations and 592.3 kcal/mol from experiments at 298 K), compressibility (0.0177−0.0194 GPa^{-1} from the $\langle P\rangle-\langle V\rangle$ curve obtained from a series of MDs at 11 different pressures at 298 K and 0.0170−0.0192 GPa^{-1} from experiments), and vibrational spectra of the $BaSO_4$ crystal. This FF in combination with the F3C FF for water[91] reproduces reasonably well the snap binding energies and interatomic distances of $Ba(H_2O)_8^{2+}$ and $(SO_4)(H_2O)_6^{2-}$ clusters determined from QM calculations (B3LYP/LACVP*) and should describe properly the interaction between $BaSO_4$ and water.

TABLE 21: QM and FF Calculations for $Ba(H_2O)_8^{2+}$ [a]

	QM (B3LYP/LACVP**++)[a]		
	before CP	after CP	FF
snap BE	237.0	233.6	237.0
optimum $r(Ba-O_w)$ (Å)	3.01		3.02

[a] The 6-31G**++ basis set was used for S, O, and H.

TABLE 22: QM and FF Calculations for $(SO_4)(H_2O)_6^{2-}$ [a]

	QM (B3LYP/LACVP**++)[a]		QM(LMP2)[a]	
	before CP	after CP	before CP	FF
snap BE	159.1	150.1	155.3	157.8
$r(S-O_w)$ (Å)	3.48			3.53
$r(O-O_w)$ (Å)	2.88			2.93
$r(S-H_w)$ (Å)	2.93			2.99
$r(O-H_w)$ (Å)	2.02			2.07

[a] The 6-31G**++ basis set was used for S, O, and H.

TABLE 23: Surface Energies of Barite−Water Interfaces at 298 K, Which Were Calculated from 80-ps MD Simulations with FF Developed to Fit to Higher-Level QM (B3LYP/LACVP++)**

surface	(210)	(001)	(010)	(100)
E(composite) (kcal/mol)[a]	−19575	−19550	−19525	−19549
$\Delta E/2$ (kcal/mol)[a]	89	102	114	102
surface area (Å^2)	198	194	246	160
surface energy (mJ/m^2)	311	364	321	443

[a] E(reference system) = E(bulk water) + E(bulk barite) = −19753 ± 6 kcal/mol.

Using this combination of MSXX FF and F3C FF, the surface energies for (210), (100), (010), and (001) surfaces of $BaSO_4$ were examined both in a vacuum and in the presence of water layers in contact with them.

The vacuum MD calculations at 298 K give the same sequence of surface energies as reported in the previous MM calculation of Allan and co-workers.[30] Our calculations also indicate that a smaller degree of structural change is expected after the generation of the (001) surface than for the other three, explaining why the (001) surface is the only surface that can be cut clean and stable.

In water, the MD calculations at 298 K do *not* give the same sequence of surface energies as implied from the experimental morphology data (assuming lower surface energy for larger surface area). However, the surface energy (a thermodynamic property) might not be the exclusive factor to determine the morphology of crystals. Thus, we estimated the crystal growth rate in the direction of each surface normal from the energy change accompanying the transition from a full-monolayer surface to a half-monolayer surface representing the midpoint of the layer-by-layer growth of the surface (higher energy change for slower growth and in turn for larger surface area). Indeed, this gives a closer, though not perfect, agreement with experiments.

This MSXX FF should be suitable for studying the effects of various scale inhibitors and scale dissolvers for $BaSO_4$. We will report results[102] that the efficacy of scale dissolution simulated using this FF does correlate with current experimental data.

In the process of developing the FF for $BaSO_4$, we also developed FF's for $SrSO_4$ and $CaSO_4$. The FF and various properties for these systems are included in Appendix A.

Acknowledgment. The research was funded by grants from Chevron Petroleum Technology Company and NSF (CHE 99-

TABLE A1: Force Field Parameters for MSO_4 (M = Sr and Ca)[a]

$E^{coulomb}$	Q(M)	2.0|e|				
E^{vdW}	R_o(Sr)[b]	5.920	D_o(Sr)[c]	0.004	ζ(Sr)	16.0
	R_o(Ca)[b]	4.338	D_o(Ca)[c]	0.110	ζ(Ca)	12.5

[a] For functional forms, see Table 6. [b] In Å. [c] In kcal/mol.

TABLE A2: Densities (g/cm^3) and Cell Parameters (Å) of $SrSO_4$ and $CaSO_4$

	cell parameters		density	
	calcd	expt[a]	calcd	expt[a]
$SrSO_4$	(8.236, 5.502, 6.781)	(8.360, 5.352, 6.858)	3.976	3.976
$CaSO_4$	(6.901, 6.851, 6.465)	(6.993, 6.995, 6.245)	2.963	2.960

[a] References 103 and 104.

TABLE A3: Lattice Energies (kcal/mol) of MSO_4 (M = Sr and Ca) at 298 K Calculated from MM at 0 K with Correction for Room Temperature

	calculation					expt[b]
	$E_{MM,0K}$	ZPE	$\Delta H_{0\rightarrow 298K}$	$\Delta H^0_{f,298K}$[a]	ΔH_{latt}[a]	ΔH_{latt}
$SrSO_4$	−619.94	11.954	4.442	−603.54	619.24	619 (±12)
$CaSO_4$	−647.73	12.599	4.017	−631.11	646.81	647 (±12)

[a] $\Delta H^0_{f,298K}(SO_4) = 14.217$ kcal/mol; $\Delta H^0_{f,298K}(M) = 1.480$ kcal/mol. [b] See Table 3.

TABLE A4: Compressibilities χ (GPa^{-1}) of $SrSO_4$ and $CaSO_4$

	calculation			experiment		
	MM (0 K)[a]	several MDs (298 K)[b]	one MD (298 K)[c]	*d*	*e*	*f*
$SrSO_4$	0.0168	0.0182	0.0161	0.0122	0.0159	
$CaSO_4$	0.0155	0.0204	0.0182		0.0184	0.0191 0.0173

[a] From second derivative of energy with respect to volume at 0 K. [b] From the linear fit of $\langle P\rangle-\langle V\rangle$ plot obtained from MDs at $P = -0.5$, -0.3, -0.1, 0.0, 0.1, 0.3, and 0.5 (in GPa) during 100 ps after 100-ps equilibration. [c] From the fluctuation of volume during final 100 ps out of 200-ps MD at 298 K. [d] References 58 and 59. [e] Reference 53. [f] Reference 54. 0.0191 from **s** and 0.0173 from **c**.

85574 and 99-77872). In addition, the facilities of the MSC are also supported by grants from DOE-ASCI-ASAP, ARO-MURI, ARO-DURIP, Dow Chemical, 3M, Beckman Institute, Avery-Dennison, Chevron Corporation, Seiko Epson, Asahi Chemical, and Kellogg's.

Appendix A. Strontium Sulfate ($SrSO_4$) and Calcium Sulfate ($CaSO_4$)

The FF's for $SrSO_4$ and $CaSO_4$ (Table A1) were determined in the same way as for $BaSO_4$ to reproduce the experimental data for bulk crystals. The results are reported in Tables A2−A4.

Appendix B. NPT Simulations with F3C Water Potential[91]

The density, potential energy, and RDFs (O−O, O−H, and H−H) of a water bath of 267 water molecules were calculated from a 200-ps NPT MD simulation at 298 K using the F3C water potential[91] with the Ewald method (see section 5 for the details of the F3C potential). All of the properties were estimated by taking averages over the last 100 ps of the simulation.

The density was estimated as 1.00 ± 0.01 g/cm^3 (Figure B1) and this is in good agreement with the experimental density of 0.997 g/cm^3 at 298 K.[105]

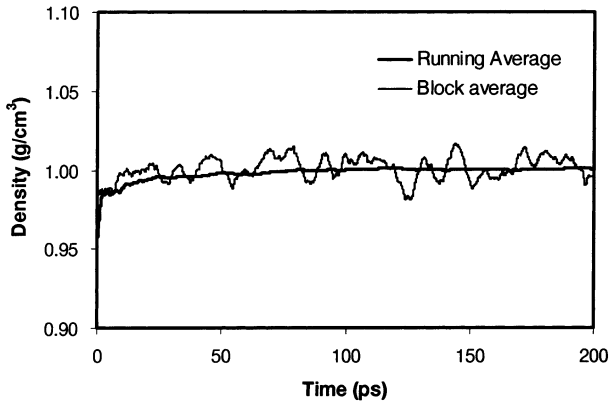

Figure B1. Density (g/cm^3) of a water bath calculated as a function of time (ps).

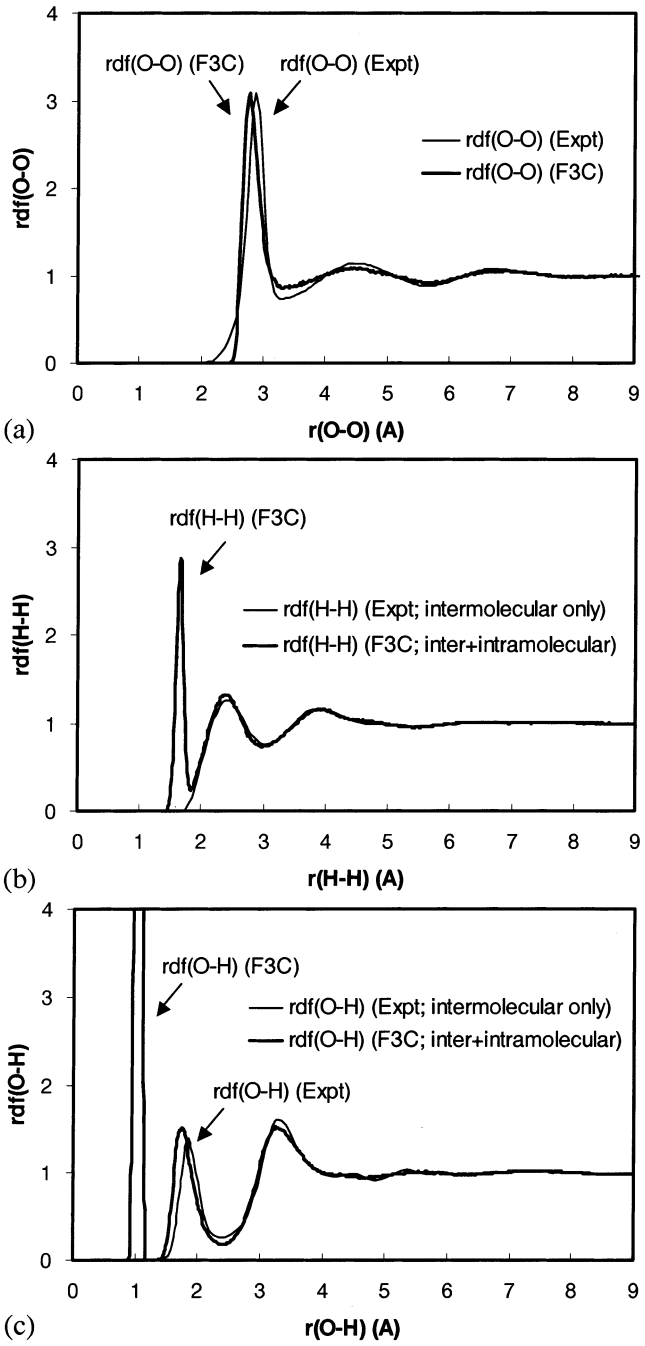

Figure B2. RDFs in water at 298 K. Calculation versus experiment. (a) O−O, (b) H−H, and (c) O−H.

TABLE B1: Characteristics of the O−O RDFs in Water

	first peak		first valley		second peak	
	position	height	position	height	position	height
expt[a]	2.88 Å	3.092	3.33 Å	0.734	4.48 Å	1.136
F3C (NVT)	2.79 Å	3.099	3.31 Å	0.827	4.43 Å	1.092
F3C (NPT)	2.77 Å	3.092	3.31 Å	0.850	4.41 Å	1.082

[a] From the neutron scattering experiment at 25 °C. Reference 106.

TABLE B2: Potential Energy Per Water Molecule (U_{pot}; kcal/mol)

FF	temp (K)	U_{pot}	other FFs	temp (K)	U_{pot}
F3C (NVT)	298	−10.18	RCF[a]	302	−9.5
F3C (NPT)	298	−10.18	TIP3P[a]	298	−9.9
expt[a]	298	−9.9	SPC[a]	298	−10.2
			SPC/E[a]	300	−10.8
			Ferguson[b]	298	−10.0

[a] Taken from ref 91. [b] Taken from ref 107.

The calculated O−O RDF also reproduces the overall features of the RDF obtained from the neutron scattering experiment (Table B1 and Figure B2a). However, the first peaks of both simulations are slightly (∼0.1 Å) shifted toward the denser packing of the neighbors compared with the experimental RDF. The simulation also reproduces the overall features of experimental RDFs for O−H and for H−H as well (Figures B2b and B2c).

The potential energy per water molecule was estimated as −10.18 kcal/mol, which is in reasonable agreement with experiment and the results from other model potentials for water (Table B2).

Appendix C. Comparison with Force Field from Allan and Co-workers[30]

Allan's FF (Tables C1−C2) has several common features with ours with several significant differences:

TABLE C1: Allan and Co-workers' Force Field for $BaSO_4$[a]

$$E = E^{\text{nonbond}} + E^{\text{valence}} = [E^{\text{coulomb}} + E^{\text{vdW}}] + [E^{\text{bond}}_{\text{SO}} + E^{\text{angle}}_{\text{OSO}}]$$

$$E^{\text{coulomb}}_{\text{ij}}(R) = C_0\frac{q_i q_j}{\epsilon R_{\text{ij}}}$$

$$E^{\text{vdW}}_{\text{ij}}(R) = D_0\left\{\left[\left(\frac{6}{\varsigma-6}\right)e^{\varsigma(1-R/R_0)}\right] - \left[\left(\frac{\varsigma}{\varsigma-6}\right)\left(\frac{R_0}{R}\right)^6\right]\right\} = A\exp\left(-\frac{R}{\rho}\right) - \frac{C}{R^6}$$

$$E^{\text{bond}}_{\text{SO}}(R) = D_e(\{1 - e^{-\beta(R-R_0)^2}\} - 1)$$

$$E^{\text{angle}}_{\text{OSO}}(\theta) = \frac{1}{2}K_\theta(\theta - \theta_0)^2$$

[a] The constants in E^{coulomb} are the dielectric constant (ϵ) and $C_0 = 332.0637$ (the unit conversion factor when atomic charges q_i's are in electron units ($|e|$), the distance R is in Å, and E^{coulomb} is in kcal/mol).

TABLE C2: Allan's FF Parameters for $BaSO_4$[a]

E^{coulomb}(Ba)	q^b	2.00 (2.000)				
E^{coulomb}(S)	q^b	1.36 (1.544)				
E^{coulomb}(O)	q^b	−0.84 (−0.886)				
E^{vdW}(O−O)	ρ^c	0.2000 (0.25251)	A^d	2388720 (55000)	C^e	599.1 (269)
	$R_o{}^c$	3.288 (3.4046)	$D_o{}^d$	0.3012 (0.0957)	ζ	16.44 (13.483)
E^{vdW}(Ba−O)[h]	ρ^c	0.2907 (0.305)	A^d	97403.9 (46000)	C^e	0 (230)
	$R_o{}^c$	5.2326 (6.942)	$D_o{}^d$	0.001483 (0.0012)	ζ	18.0 (18.0)
E^{bond}(S−O)	$R_o{}^c$	1.505	$D_e{}^d$	115.302	β^e	1.2
E^{angle}(O−S−O)	$\theta_o{}^f$	109.47	$K_\theta{}^g$	345.908		

[a] Reference 30. For functional forms, see Table C1. Our MSXX FF parameters are shown in parentheses. [b] In $|e|$. [c] In Å. [d] In kcal/mol. [e] In kcal/mol/Å^6. [f] In degrees. [g] In kcal/mol/rad^2. [h] Among infinite number of three-paremeter set (R_o, D_o, and ζ) of our exponential form matching the two-parameter (ρ and A), purely repulsive form of Allan, we chose a set with the same ζ as ours.

TABLE C3: Density and Cell Parameters of $BaSO_4$ Calculated with Allan's FF

	MM (0 K)	MD (298 K)	expt (298 K)[a]
a (Å)	8.888	8.941 ± 0.001	8.8842
b (Å)	5.470	5.507 ± 0.002	5.4559
c (Å)	7.142	7.188 ± 0.008	7.1569
α (°)	90	89.99 ± 0.03	90
β (°)	90	89.99 ± 0.01	90
γ (°)	90	90.01 ± 0.02	90
density (g/cm^3)	4.464 (4.531)[b]	4.384 ± 0.004 (4.473)[b]	4.474

[a] References 38 and 39. [b] From our FF.

TABLE C4: Lattice Energy (kcal/mol) Per $BaSO_4$ Unit Calculated with Allan's FF at 298 K

	MM with corrections to 298 K				MD (298 K)	expt
	$E_{\text{MM,0K}}$	ZPE	$\Delta H_{0\rightarrow 298K}$	$\Delta H^0_{\text{f,298K}}$	⟨PE⟩	(298 K)
$BaSO_4$	−585.94	10.55	4.54	−570.85	−580.40 ± 0.07	
$SO_4{}^{2-}$	0	8.034	3.2976	11.332	2.65 ± 0.04	
Ba^{2+}	0	0	1.48[a]	1.48	0.888[b]	
$\Delta H_{\text{latt,298K}}$				583.66 (592.96)[c]	583.94 (591.6)[c]	592.3[d]

[a] 2.5 *RT*. [b] 1.5 *RT*. [c] From our FF. [d] See Table 3.

TABLE C5: Compressibility χ (GPa^{-1}) of $BaSO_4$ Calculated with Allan's FF

	2nd derivative	MDs at 298 K	MD at 298 K		
method	(0 K)	linear fit	adiabatic	isothermal	expt
χ	0.01771[a]	0.01971[b]	0.02704[c]	0.02815[c]	0.0170−0.0192[d]

[a] From second derivative of energy with respect to volume at 0 K. [b] From the linear fit of ⟨P⟩−⟨V⟩ plot (Figure C1). [c] From the fluctuation of volume during final 250 ps out of 300-ps MD at 298 K. [d] See Table 4.

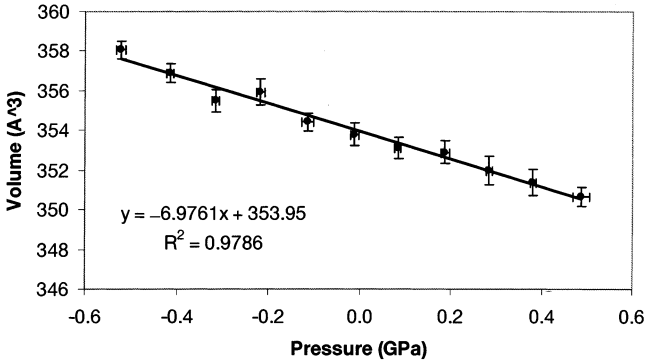

Figure C1. ⟨P⟩−⟨V⟩ curve used to estimate compressibility from its slope at $P = 0.0001$ GPa. ⟨P⟩ and ⟨V⟩ are the average values during a 350-ps MD simulation using Allan's FF after a 50-ps equilibration. The errors were estimated from the standard deviation between 14 block-averages during each 25-ps block. The slope was taken from the first-order (linear) fit.

(1) The Allan's parameters were adjusted to reproduce experimental data: structure and elastic properties, but not energetic properties.

(2) Allan compared the results based on minimization at 0 K with experimental data measured at room temperature (we compare MD with experiments at the same temperature).

(3) We both use the formal charges on Ba^{2+} and $SO_4{}^{2-}$ to estimate the Coulombic interaction.

(4) Allan included vdW interactions only for the O−O and Ba−O pairs, but not for Ba−Ba, Ba−S, S−S, or S−O pairs. They use the same exponential-6 form as ours for the O−O interaction, but they use purely repulsive form for the Ba−O interaction.

(5) The valence part of the Allan's FF uses bond-stretching and angle-bending terms but no cross terms between them.

Using Allan's FF, the structure, the cohesive energy, and the compressibility of $BaSO_4$ were calculated from MD at 298 K in the same manner as done with our FF above. They are listed in Table C3−C5, respectively, along with the experimental data and the results with our FF.

References and Notes

(1) Yuan, M. D.; Todd, A. C.; Sorbie, K. S. *Mar. Petrol. Geol.* **1994**, *11*, 24.
(2) Todd, A. C.; Yuan, M. D. *SPE Prod. Eng.* **1990**, August, 279.
(3) Todd, A. C.; Yuan, M. D. *SPE Prod. Eng.* **1992**, February, 85.
(4) Raju, K.; Atkinson, G. *J. Chem. Eng. Data* **1988**, *33*, 490.
(5) Raju, K. U. G.; Atkinson, G. *J. Chem. Eng. Data* **1989**, *34*, 361.
(6) Raju, K. U. G.; Atkinson, G. *J. Chem. Eng. Data* **1990**, *35*, 361.
(7) Morris, R. L.; Paul, J. M. U.S. Patent, No. 5,049,297, 1991.
(8) Blount, C. W. *Am. Mineral.* **1977**, *62*, 942.
(9) Paul, J. M.; Morris, R. L. U.S. Patent, No. 5,093,020, 1992.
(10) Putnis, A.; Putnis, C. V. *SPE Int. Symp. Oil Field Chem. 29094* **1995**, February, 773.
(11) Archibald, D. D.; Gaber, B. P.; Hopwood, J. D.; Mann, S.; Boland, T. *J. Cryst. Growth* **1997**, *172*, 231.
(12) Pina, C. M.; Becker, U.; Risthaus, P.; Bosbach, D.; Putnis, A. *Nature* **1998**, *395*, 483.
(13) Pina, C. M.; Bosbach, D.; Prieto, M.; Putnis, A. *J. Cryst. Growth* **1998**, *187*, 119.
(14) Higgins, S. R.; Jordan, G.; Eggleston, C. M.; Knauss, K. G. *Langmuir* **1998**, *14*, 4967.
(15) Bosbach, D.; Hall, C.; Putnis, A. *Chem. Geol.* **1998**, *151*, 143.
(16) Putnis, A.; Junta-Rosso, J. L.; Hochella, M. F., Jr. *Geochim. Cosmochim. Acta* **1995**, *59*, 4623.
(17) Dunn, K.; Daniel, E.; Shuler, P. J.; Chen, H. J.; Tang, Y.; Yen, T. F. *J. Colloid Interface Sci.* **1999**, *214*, 427.
(18) Dunn, K. Study of chemical dissolution for controlling barium sulfate scale deposit. Ph.D. Thesis, University of Southern California, Los Angeles, CA, 1999.
(19) Wang, K. S.; Resch, R.; Dunn, K.; Shuler, P. J.; Tang, Y.; Koel, B. E.; Yen, T. F. *Langmuir* **2000**, *16*, 649.
(20) Wang, K. S.; Resch, R.; Shuler, P. J.; Tang, Y.; Chen, H. J.; Koel, B. E.; Yen, T. F. *J. Colloid Interface Sci.* **1999**, *219*, 212.
(21) Wang, K.-S.; Resch, R.; Dunn, K.; Shuler, P.; Tang, Y.; Koel, B. E.; Yen, T. F. *Colloids Surf. A* **1999**, *160*, 217.
(22) Black, S. N.; Bromley, L. A.; Cottier, D.; Davey, R. J.; Dobbs, B.; Rout, J. E. *J. Chem. Soc., Faraday Trans.* **1991**, *87*, 3409.
(23) Davey, R. J.; Black, S. N.; Bromley, L. A.; Cottier, D.; Dobbs, B.; Rout, J. E. *Nature* **1991**, *353*, 549.
(24) Benton, W. J.; Collins, I. R.; Grimsey, I. M.; Parkinson, G. M.; Rodger, S. A. *Faraday Discuss.* **1993**, *95*, 281.
(25) Bromley, L. A.; Cottier, D.; Davey, R. J.; Dobbs, B.; Smith, S.; Heywood, B. R. *Langmuir* **1993**, *9*, 3594.
(26) van der Leeden, M. C.; van Rosmalen, G. M. *J. Colloid Interface Sci.* **1995**, *171*, 142.
(27) Heywood, B. R.; Mann, S. *J. Am. Chem. Soc.* **1992**, *114*, 4681.
(28) Hartman, P.; Perdok, W. G. *Acta Crystallogr.* **1955**, *8*, 525.
(29) Hartman, P.; Strom, C. S. *J. Cryst. Growth* **1989**, *97*, 502.
(30) Allan, N. L.; Rohl, A. L.; Gay, D. H.; Catlow, C. R. A.; Davey, R. J.; Mackrodt, W. C. *Faraday Discuss.* **1993**, 273.
(31) Parker, S. C.; Kelsey, E. T.; Oliver, P. M.; Titiloye, J. O. *Faraday Discuss.* **1993**, *95*, 75.
(32) Rohl, A. L.; Gay, D. H.; Davey, R. J.; Catlow, C. R. A. *J. Am. Chem. Soc.* **1996**, *118*, 642.
(33) Redfern, S. E.; Parker, S. C. *J. Chem. Soc., Faraday Trans.* **1998**, *94*, 1947.
(34) Woensdregt, C. F. *Faraday Discuss.* **1993**, 97.
(35) Gay, D. H.; Rohl, A. L. *J. Chem. Soc., Faraday Trans.* **1995**, *91*, 925.
(36) Blanco, M.; Tang, Y.; Shuler, P.; Goddard, W. A., III. *Mol. Eng.* **1997**, *7*, 491.
(37) Rohl, A. L.; et al. *Faraday Discuss.* **1993**, *95*, 367.
(38) Dove, P. M.; Czank, C. A. *Geochim. Cosmochim. Acta* **1995**, *59*, 1907.
(39) Hill, R. J. *Can. Mineral.* **1977**, *15*, 522.
(40) *CRC Handbook of Chemistry and Physics*, 80th ed.; CRC Press: Boca Raton, FL, 1999−2000.
(41) Wagman, D. D.; Evans, W. H.; Parker, V. B.; Schumm, R. H.; Halow, I.; Bailey, S. M.; Churney, K. L.; Nuttall, R. L. *J. Phys. Chem. Ref. Data* **1982**, *11*, Supp. No. 2.
(42) Marcus, Y. *Ion Solvation*; John Wiley and Sons: New York, 1985.
(43) Vasil'ev, V. P.; Zolotarev, E. K.; Kapustinskii, A. F.; Mishchenko, K. P.; Podgornaya, E. A.; Yatsimirskii, K. B. *Russ. J. Phys. Chem.* **1960**, *34*, 840.
(44) Noyes, R. M. *J. Am. Chem. Soc.* **1962**, *84*, 513.
(45) Lim, C.; Bashford, D.; Karplus, M. *J. Phys. Chem.* **1991**, *95*, 5610.
(46) Grunwald, E.; Steel, C. *Int. Rev. Phys. Chem.* **1996**, *15*, 273.
(47) Kebarle, P.; Searles, S. K.; Zolla, A.; Scarborough, J.; Arshadi, M. *J. Mass Spectrom.* **1997**, *32*, 915.
(48) Tissandier, M. D.; Cowen, K. A.; Feng, W. Y.; Gundlach, E.; Cohen, M. H.; Earhart, A. D.; Coe, J. V.; Tuttle, T. R., Jr. *J. Phys. Chem. A* **1998**, *102*, 7787.
(49) Ladd, M. F. C.; Lee, W. H. *J. Inorg. Nucl. Chem.* **1968**, *30*, 330.
(50) Ladd, M. F. C.; Lee, W. H. *J. Inorg. Nucl. Chem.* **1961**, *21*, 216.
(51) Jenkins, H. D. B. *Mol. Phys.* **1975**, *30*, 1843.
(52) Mott, N. F.; Jones, H. *The Theory of the Properties of Metals and Alloys*; Dover Publications: New York, 1975; p 15.
(53) Adams, A. H. In *Compressibility of crystalline compounds, minerals and rocks*; Washburn, E. W., Ed.; National Research Council and McGraw-Hill Book Company, Inc.: New York, 1928; Vol. III, p 49.
(54) Schwerdtner, W. M.; Tou, J. C.-M.; Hertz, P. B. *Can. J. Earth Sci.* **1965**, *2*, 673.
(55) Haussühl, S. *Z. Kristallogr.* **1993**, *205* (Pt. 2), 215.
(56) *Landolt-Bornstein, Numerical Data and Functional Relationships in Science and Technology, New Series III, 11*; Springer: Berlin, 1979.
(57) Haussühl, S. *Z. Kristallogr.* **1990**, *192*, 137.
(58) Seshagiri Rao, T. *Proc. Indian Acad. Sci. Sect. A* **1951**, *33*, 251.
(59) Hearmon, R. F. S. *Adv. Phys.* **1956**, *5*, 323.
(60) Voigt, W. *Lehrbuch der Kristallphysik*; B. G. Teubner: Leipzig, Germany, 1928; p 179.
(61) Voigt, W. *Lehrbuch der Kristallphysik*; B. G. Teubner: Leipzig, Germany, 1928; p 761.
(62) Jayarama Reddy, P.; Subrahmanyam, S. V. *Proc. Indian Acad. Sci. Sect. A* **1959**, *50*, 380.
(63) Hearmon, R. F. S. *Rev. Mod. Phys.* **1946**, *18*, 409.
(64) Voigt, W. *Lehrbuch der Kristallphysik*; B. G. Teubner: Leipzig, Germany, 1928.
(65) Jayasooriya, U. A.; Kettle, S. F. A.; Mahasuverachai, S.; Al-Jowder, O. *J. Chem. Phys.* **1991**, *94*, 5946.
(66) Dawson, P.; Hargreave, M. M.; Wilkinson, G. R. *Spectrochim. Acta* **1977**, *33A*, 83.
(67) Hezel, A.; Ross, S. D. *Spectrochim. Acta* **1966**, *22*, 1949.
(68) Tarte, P.; Nizet, G. *Spectrochim. Acta* **1964**, *20*, 503.
(69) Vassallo, A. M.; Finnie, K. S. *Appl. Spectrosc.* **1992**, *46*, 1477.
(70) Schroeder, R. A.; Lippincott, E. R.; Weir, C. E. *J. Inorg. Nucl. Chem.* **1966**, *28*, 1397.
(71) Mayo, S. L.; Olafson, B. D.; Goddard, W. A., III. *J. Phys. Chem.* **1990**, *94*, 8897.
(72) Karasawa, N.; Dasgupta, S.; Goddard, W. A., III. *J. Phys. Chem.* **1991**, *95*, 2260.
(73) Dasgupta, S.; Smith, K. A.; Goddard, W. A., III. *J. Phys. Chem.* **1993**, *97*, 10891.
(74) Karasawa, N.; Goddard, W. A., III. *Macromolecules* **1992**, *25*, 7268.
(75) Dasgupta, S.; Hammond, W. B.; Goddard, W. A., III. *J. Am. Chem. Soc.* **1996**, *118*, 12291.
(76) *Jaguar V3.0*; Schrödinger, Inc. For the CHELP-type ESP charges, see: (a) Chirlian, L. E.; Francl, M. M. *J. Comput. Chem.* **1987**, *8*, 894. (b) Woods, R. J.; Khalil, M.; Pell, W.; Moffat, S. H.; Smith, V. H., Jr. *J. Comput. Chem.* **1990**, *11*, 297. (c) Breneman, C. M.; Wiberg, L. B. *J. Comput. Chem.* **1990**, *11*, 361. For the effective core potentials, see: (d) Hay, P. J.; Wadt, W. R. *J. Chem. Phys.* **1985**, *82*, 284. (e) Hay, P. J.; Wadt, W. R. *J. Chem. Phys.* **1985**, *82*, 299.
(77) Tannor, D. J.; Marten, B.; Murphy, R.; Friesner, R. A.; Sitkoff, D.; Nicholls, A.; Ringnalda, M.; Goddard, W. A., III; Honig, B. *J. Am. Chem. Soc.* **1994**, *116*, 11875.
(78) Marten, B.; Kim, K.; Cortis, C.; Friesner, R. A.; Murphy, R. B.; Ringnalda, M. N.; Sitkoff, D.; Honig, B. *J. Phys. Chem.* **1996**, *100*, 11775.
(79) Honig, B.; Sharp, K.; Yang, A.-S. *J. Phys. Chem.* **1993**, *97*, 1101.
(80) Honig, B.; Nicholls, A. *Science* **1995**, *268*, 1144.
(81) Nicholls, A.; Honig, B. *J. Comput. Chem.* **1991**, *12*, 435.
(82) Parker, S. C.; et al. *Faraday Discuss.* **1993**, *95*, 145.
(83) Rappé, A. K.; Casewit, C. J.; Colwell, K. S.; Goddard, W. A., III; Skiff, W. M. *J. Am. Chem. Soc.* **1992**, *114*, 10024.
(84) *Cerius2 3.5*; Molecular Simulations Inc.
(85) Hoover, W. G. *Phys. Rev. A* **1985**, *31*, 1695.
(86) Nosé, S. *J. Chem. Phys.* **1984**, *81*, 511.
(87) Nosé, S. *Mol. Phys.* **1984**, *52*, 255.
(88) Karasawa, N.; Goddard, W. A., III. *J. Phys. Chem.* **1989**, *93*, 7320.
(89) Decius, J. C.; Hexter, R. M. *Molecular Vibrations in Crystals*; McGraw-Hill, Inc.: New York, 1977.
(90) *Polygraf*; Molecular Simulations, Inc.
(91) Levitt, M.; Hirshberg, M.; Sharon, R.; Laidig, K. E.; Daggett, V. *J. Phys. Chem. B* **1997**, *101*, 5051.
(92) Rahman, A.; Stillinger, F. H. *J. Chem. Phys.* **1971**, *55*, 3336.

(93) Stillinger, F. H.; Rahman, A. *J. Chem. Phys.* **1974**, *60*, 1545.
(94) Berendsen, H. J. C.; Postma, J. P. M.; van Gunsteren, W. F.; Hermans, J. In *Intermolecular forces*; Pullman, B., Ed.; D. Reidel Publishing Company: Dordrecht, The Netherlands, 1981; p 331.
(95) Jorgensen, W. L.; Chandrasekhar, J.; Madura, J. D.; Impey, R. W.; Klein, M. L. *J. Chem. Phys.* **1983**, *79*, 926.
(96) Jorgensen, W. L. *J. Am. Chem. Soc*. **1981**, *103*, 335.
(97) Berendsen, H. J. C.; Grigera, J. R.; Straatsma, T. P. *J. Phys. Chem.* **1987**, *91*, 6269.
(98) Marcus, Y. *Chem. Rev.* **1988**, *88*, 1475.
(99) Ohtaki, H.; Radnal, T. *Chem. Rev.* **1993**, *93*, 1157.
(100) Albreight, J. N. *J. Chem. Phys.* **1972**, *56*, 3783.
(101) Dove, P. M.; Platt, F. M. *Chem. Geol*. **1996**, *127*, 331.
(102) Jang, Y. H.; Blanco, M.; Tang, Y.; Shuler, P.; Goddard, W. A., III. To be submitted.
(103) Hawthorne, F. C.; Ferguson, R. B. *Can. Mineral*. **1975**, *13*, 181.
(104) Hawthorne, F. C.; Ferguson, R. B. *Can. Mineral*. **1975**, *13*, 289.
(105) Kell, G. C. *J. Chem. Eng. Data* **1967**, *12*, 66.
(106) Soper, A. K.; Phillips, M. G. *Chem. Phys.* **1986**, *107*, 47.
(107) Ferguson, D. M. *J. Comput. Chem.* **1995**, *16*, 501.